Rep. Prog. Phys. **63** (2000) 1933–1995. Printed in the UK PII: S0034-4885(00)85025-3

Time-reversed acoustics

Mathias Fink, Didier Cassereau, Arnaud Derode, Claire Prada, Philippe Roux, Mickael Tanter, Jean-Louis Thomas and François Wu

Laboratoire Ondes et Acoustique, Ecole Supérieure de Physique et de Chimie Industrielle de la Ville de Paris, Université Denis Diderot, UMR CNRS 7587, 10 Rue Vauquelin, 75005 Paris, France

Received 24 November 1999

Abstract

The objective of this paper is to show that time reversal invariance can be exploited in acoustics to create a variety of useful instruments as well as elegant experiments in pure physics.

Section 1 is devoted to the description of time reversal cavities and mirrors together with a comparison between time reversal and phase conjugation. To illustrate these concepts, several experiments conducted in multiply scattering media, waveguides and chaotic cavities are presented in section 2. Applications of time reversal mirrors (TRMs) in hydrodynamics are then presented in section 3. Section 4 is devoted to the application of TRMs in pulse echo detection. A complete theory of the iterative time reversal mode is presented. It will be explained how this technique allows for focusing on different targets in a multi-target medium. Another application of pulse echo TRMs is presented in this section: how to achieve resonance in an elastic target? Section 5 explores the medical applications of TRMs in ultrasonic imaging, lithotripsy and hyperthermia and section 6 shows the promising applications of TRMs in nondestructive testing of solid samples.

0034-4885/00/121933+63$90.00

Contents

Introduction

The objective of this paper is to show that time reversal (TR) invariance, a fundamental symmetry that holds nearly everywhere in microscopic physics, can be exploited in macroscopic physics to create a variety of useful instruments as well as elegant experiments in pure physics. It is in the field of acoustic wave phenomena that macroscopic TR invariance holds, to the extent that everything is adiabatic.

Although classical mechanics equations are reversible on the microscopic scale, it is difficult to test the TR invariance of a complex system of particles. It requires introducing a 'mirror' of the time variable. In the world of images, such a mirror exists by taking a motion picture of the system and then running the film backwards. In the real world, the reversal of the motion in a complex system can be ascribed to a change in initial conditions. If we want to reconstruct an exploded block from the various scattered pieces, a time reversal mirror (TRM) would be a device interacting with the pieces when they cross a closed surface surrounding the initial block, measuring their arrival time and velocity. Thereafter, at the appropriate time, the system applies a velocity of the same speed, but opposite direction, to each piece which then returns to its starting position. To reconstruct the block, one would have to first send back the slowest pieces, which had arrived last. Such a device, however, would rely on its ability to resolve the details of every particle's dynamics with adequate precision. But, the extreme sensitivity to initial conditions in nonlinear dynamics explains that any slight errors in the measurement make such TR experiments impossible.

In linear wave physics, however, the amount of information needed to describe a wavefield without ambiguity is limited. It depends on the shortest wavelength of the field. The smallest scale of the wavefield fluctuations is on the order of the wavelength. Moreover, in linear physics a small error in the initial conditions has only small consequences in the system evolution. Thus TR experiments with wavefields can be made, given adequate reversible sensor technology (transmit–receive mode). The measurement of the particles velocity is then replaced by the measurement of the wavefield, and the application of forces is replaced by the radiation of a new wavefield.

Such conditions are available in acoustics by using *reversible acoustic retina* arrays of piezoelectric transducers that combine the capabilities of microphone and loudspeaker. Within the range of sonic or ultrasonic frequencies where adiabatic processes dominate, the acoustic pressure field is described by a scalar $p(\vec{r}, t)$ that, within a heterogeneous propagation medium of density $\rho(\vec{r})$ and compressibility $\kappa(\vec{r})$, satisfies the equation

$$\begin{aligned} &(L_r + L_t)\, p(\vec{r}, t) = 0, \\ &L_r = \vec{\nabla}\cdot\left(\frac{1}{\rho(\vec{r})}\vec{\nabla}\right), \qquad L_t = -\kappa(\vec{r})\partial_{tt}. \end{aligned} \tag{1}$$

This equation is TR invariant because L_t contains only second-order derivatives with respect to time (self-adjoint in time). This means that for every burst of sound $p(\vec{r}, t)$ diverging from a source—and possibly reflected, refracted or scattered by any propagation media—there exists in theory a set of waves $p(\vec{r}, -t)$ that precisely retraces all of these complex paths and converges in synchrony at the original source, as if time were going backwards. Note that the spatial part L_r of this equation is also self-adjoint in space and thus satisfies spatial reciprocity (interchanging the source and the receiver does not alter the resulting field).

Recently, taking advantage of these two properties, the concept of a TR cavity (TRC) has been developed and several devices have been built which illustrate the feasibility of this concept [1–3]. In such a device (see section 1) an acoustic source, located inside a

heterogeneous lossless medium, radiates a brief transient pulse that propagates through and is distorted by the medium. If the acoustic field can be measured on every point of a closed surface surrounding the medium, and retransmitted through the medium in a time-reversed chronology, then the wave will travel back to its source and recover its original shape. Spatial reciprocity [4] is required to reconstruct the exact time-reversed wave in the whole volume by means of a two-dimensional TR operation. From an experimental point of view, a TRC consists of a two-dimensional piezoelectric transducer array that samples the wavefield over a closed surface. An array pitch of the order of $\lambda/2$ where λ is the smallest wavelength of the pressure field is needed to ensure the recording of all the information on the wavefield. Each transducer is connected to its own electronic circuitry that consists of a receiving amplifier, an A/D converter, a storage memory and a programmable transmitter able to synthesize a time-reversed version of the stored signal. In practice, TRCs are difficult to realize and the TR operation is usually performed on a limited angular area, thus limiting reversal and focusing quality. A TRM consists typically of some hundred elements, or TR channels.

The basic principle of a TRM is, in some sense, an extension for broadband pulsed waves to the optical phase conjugated mirror (valid for quasi-monochromatic waves). However, this equivalence is only valid mathematically and there are some fundamental differences between these two techniques that will be described in section 1.

Section 2 will be devoted to various TR experiments conducted with TRMs. It will be shown that wave reversibility is improved if the wave traverses a multiply scattering medium before arriving on the transducer array. Through media with high-order multiple scattering, the large length of paths involved in the experiment widens the effective focusing aperture. After the TR operation, the whole multiply scattering medium behaves as a coherent focusing source, with a large angular aperture for enhanced resolution. As a consequence, in multiply scattering media, one is able to reduce the number of channels participating in the TR process. The same kind of improvement can be obtained for waves propagating in waveguides or in closed reflecting cavities. Multiple reflections along the medium boundaries significantly increase the apparent aperture of the TRM and a set of experiments conducted in waveguides and in ergodic cavities will be presented in section 2. It will be shown that for a cavity with ergodic boundary geometries a one-channel TRM is sufficient to ensure reversibility and optimal focusing.

Together, these results show the robustness of TR techniques in static media. But one can also make use of TRMs in hydrodynamics. Section 3 explores the violation of the acoustic TR invariance induced by flows and particularly by vortices. It will be shown that a double TRM works as a vortex amplifier and in this context a description of the acoustic analogue of the Aharonov–Bohm effect will be presented.

Section 4 is devoted to the application of TRMs in pulse echo detection. A complete theory of the iterative TR mode is presented together with the DORT method. It will be explained how in a multi-target medium this technique allows one to focus selectively on each target. Another application of pulse echo TRMs is presented in this section: how to resonate an elastic target?

Section 5 explores the medical applications of TRMs in ultrasonic imaging, in lithotripsy and in hyperthermia. The interesting problem of propagation through the human skull is presented. The strong ultrasonic dissipation induced by the skull breaks the TR symmetry of the wave equation and a new focusing technique that combines TR and a correction of dissipative effects is presented. As a conclusion, section 6 shows the promising applications of TRMs in nondestructive testing of solid samples.

1. Time reversal and phase conjugation

In any propagation experiment, the acoustic sources and the boundary conditions determine a unique solution $p(\vec{r}, t)$ in the fluid. The goal, in TR experiments, is to modify the initial conditions in order to generate the dual solution $p(\vec{r}, -t)$. However, due to causality requirements, $p(\vec{r}, T - t)$ is not an experimentally valid solution. Therefore, we necessarily limit ourselves to the generation of $p(\vec{r}, -t)$. Jackson and Dowling [4] and Cassereau and Fink [5] have studied theoretically the conditions necessary to ensure the generation of $p(\vec{r}, T - t)$ in the entire volume of interest.

1.1. The time reversal cavity

Although reversible acoustic retinas usually consist of discrete elements, it is convenient to examine the behaviour of idealized continuous retinas, defined by two-dimensional surfaces. In the case of a TRC, we assume that the retina completely surrounds the source. The analysis in this paragraph borrows from the backpropagation formalism [6] developed for the inverse source problem. It is important to appreciate the distinction between the backpropagation problem and the TRC problem. In both, one deals with propagation of a time-reversed field, but the propagation is real in the TRC problem and simulated in the backpropagation problem. The most important distinction, however, is that source localization methods such as backpropagation demand knowledge of the propagating medium, while the TRC method does not.

The basic TR experiment can be described in the following way. In a first step, a pointlike source located at $\vec{r}_0$ inside a volume V surrounded by the retina surface S emits a pulse at $t = t_0 \geqslant 0$. The wave equation is given by

$$(L_r + L_t)\, p(\vec{r}, t) = -C^{te}\delta(\vec{r} - \vec{r}_0)\delta(t - t_0) \tag{2}$$

where C^{te} is a dimensional constant that ensures the compatibility of physical units between the two sides of the equation; for simplicity, this constant will be omitted in what follows. The solution to (2) reduces to the Green function $G(\vec{r}, t|\vec{r}_0, t_0)$. Classically, $G(\vec{r}, t|\vec{r}_0, t_0)$ is written as a diverging spherical wave (homogeneous and free-space case) and additional terms that describe the interaction of the field itself with the inhomogeneities (multiple scattering) and the boundaries.

We assume that we are able to measure the pressure field and its normal derivative at any point on the surface S during the interval $[O, T]$. As TR experiments are based on a two-step process, the measurement step must be limited in time by a parameter T. In all the following, we suppose that the contribution of multiple scattering decreases with time, and that T is chosen such that the information loss can be considered as negligible inside the volume V.

During the second step of the TR process, the initial source at $\vec{r}_0$ is removed and we create on the surface of the cavity monopole and dipole sources that correspond to the TR of those same components measured during the first step. The TR operation is described by the transform $t \to T - t$ and the secondary sources are

$$\begin{aligned} &P_s(\vec{r}, t) = G(\vec{r}, T - t|\vec{r}_0, t_0), \\ &\partial_n P_s(\vec{r}, t) = \partial_n G(\vec{r}, T - t|\vec{r}_0, t_0). \end{aligned} \tag{3}$$

In this equation, ∂_n is the normal derivative operator with respect to the normal direction $\vec{n}$ to S, oriented outward. Due to these secondary sources on S, a time-reversed pressure field $p_{\mathrm{tr}}(\vec{r}_1, t_1)$ propagates inside the cavity. It can be calculated using a modified version of the

Helmoltz–Kirchhoff integral

$$p_{\mathrm{tr}}(\vec{r}_1, t_1) = \int_{-\infty}^{+\infty} \mathrm{d}t \iint_s [G(\vec{r}_1, t_1|\vec{r}, t)\partial_n p_s(\vec{r}, t) - p_s(\vec{r}, t)\partial_n G(\vec{r}_1, t_1|\vec{r}, t)] \frac{\mathrm{d}^2\vec{r}}{\rho(\vec{r})}. \tag{4}$$

Spatial reciprocity and TR invariance of the wave equation (2) yield the following expression:

$$p_{tr}(\vec{r}_1, t_1) = G(\vec{r}_1, T - t_1|\vec{r}_0, t_0) - G(\vec{r}_1, t_1|\vec{r}_0, T - t_0). \tag{5}$$

This equation can be interpreted as the superposition of incoming and outgoing spherical waves, centred on the initial source position. The incoming wave collapses at the origin and is always followed by a diverging wave. Thus the time-reversed field, observed as a function of time, from any location in the cavity, shows two wavefronts, where the second one is the exact replica of the first one, multiplied by -1.

1.2. Limitation of the time reversal process and the concept of an acoustic sink

If we assume that the retina does not perturb the propagation of the field (free-space assumption) and that the acoustic field propagates in an homogeneous fluid, the free-space Green function G reduces to a diverging spherical impulse wave that propagates with a sound speed c; it is classically written as

$$G(\vec{r}_1, t_1|\vec{r}_0, t_0) = \frac{1}{4\pi|\vec{r}_1 - \vec{r}_0|}\delta\left(t_1 - t_0 - \frac{|\vec{r}_1 - \vec{r}_0|}{c}\right).$$

Introducing this expression in (5) yields the following formulation of the time-reversed field:

$$p_{tr}(\vec{r}_1, t_1) = \delta(T - t_1 - t_0)\overset{*}{t} K(\vec{r}_1 - \vec{r}_0, t), \tag{6}$$

where $\overset{*}{t}$ is the temporal convolution operator and the kernel distribution $K(\vec{r}, t)$ is given by

$$K(\vec{r}, t) = \frac{1}{4\pi|\vec{r}|}\delta\left(t + \frac{|\vec{r}|}{c}\right) - \frac{1}{4\pi|\vec{r}|}\delta\left(t - \frac{|\vec{r}|}{c}\right). \tag{7}$$

The kernel distribution $K(\vec{r}, t)$ corresponds to the difference between two impulse spherical waves that respectively converge to and diverge from the origin of the spatial coordinate system, thus the location of the initial source. It results from this superposition that the pressure field remains finite for all time throughout the cavity, although the converging and diverging spherical waves show a singularity at the origin.

The time-reversed pressure field, observed as a function of time, shows two wavefronts, where the second one is the exact replica of the first one, multiplied by -1. If we consider a wide-band excitation function $\phi(t)$ instead of a Dirac distribution $\delta(t)$, the two wavefronts overlap near the focal point, therefore resulting in a temporal distortion of the acoustic signal. It can be shown that this distortion yields a temporal derivation of the initial excitation function at the focal point.

If we now calculate the Fourier transform of (7) over the time variable t, we obtain

$$\tilde{K}(\vec{r}, \omega) = \frac{1}{2j\pi}\frac{\sin(\omega|\vec{r}|/c)}{|\vec{r}|} = \frac{1}{j\lambda}\frac{\sin(k|\vec{r}|)}{k|\vec{r}|}, \tag{8}$$

where λ and k are the wavelength and wavenumber, respectively. As a consequence, the TR process results in a pressure field that is effectively focused on the initial source position, but with a focal spot size limited to one half-wavelength. The size of the focal spot is a direct consequence of the superposition of the two wavefronts and can be interpreted in terms of the diffraction limitations (loss of the evanescent components of the acoustic fields).

A similar interpretation can be given in the case of an inhomogeneous fluid, but the Green function G now takes into account the interaction of the pressure field with the inhomogeneities

of the medium. If we were able to create a film of the propagation of the acoustic field during the first step of the process, the final result could be interpreted as a projection of this film in the reverse order, immediately followed by a re-projection in the initial order.

The apparent failure of the time-reversed operation that leads to diffraction limitation can be interpreted in the following way: the second step described above is not strictly the TR of the first step. During the second step of an ideal time-reversed experiment, the initial active source (that injects some energy into the system) must be replaced by a sink (the TR of a source). An acoustic sink is a device that absorbs all arriving energy without reflecting it. The realization of such a sink inside a propagating medium would be very challenging because it would reduce the focal spot size below diffraction limits!!

1.3. The time reversal mirror

This theoretical model of the closed TRC is interesting since it affords an understanding of the basic limitations of the time-reversed self-focusing process; but it has some limitations, particularly when compared with an experimental setup:

- It can be proven that it is not necessary to measure and time-reverse both the pressure field and its normal derivative on the cavity surface: measuring the pressure field and re-emitting the time-reversed field in the backward direction yields the same results, on condition that the evanescent parts of the acoustic fields have vanished (propagation along several wavelengths) [7]. This comes from the fact that each transducer element of the cavity records the incoming field from the forward direction, and retransmits it (after the TR operation) in the *backward* direction (and not in the forward direction). The change between the forward and the backward direction replaces the measurement and the TR of the field normal derivative.
- From an experimental point of view, it is not possible to measure and re-emit the pressure field at any point of a 2D surface: experiments are carried out with transducer arrays that spatially sample the receiving and emitting surface. The spatial sampling of the TRC by a set of transducers may introduce grating lobes. These lobes can be avoided by using an array pitch smaller than $\lambda_{min}/2$, where λ_{min} is the smallest wavelength of the transient pressure field. In this latest case, each transducer senses all the wavevectors of the incident field.
- The temporal sampling of the data recorded and transmitted by the TRC has to be at least of the order of $T_{min}/8$ (T_{min} minimum period) to avoid secondary lobes [8].
- It is generally difficult to use acoustic arrays that completely surround the area of interest, and the closed cavity is usually replaced by a TRM of finite angular aperture. This yields an increase of the point spread function dimension that is usually related to the mirror angular aperture observed from the source.

However, in section 2, which deals with experimental results obtained with TRMs, it will be shown that the propagation medium itself can increase the total apparent aperture of the TRM, thus resulting in a focal spot size less than the one predicted by classical formulae. Three different examples will be presented (multiply scattering medium, waveguide and chaotic cavity).

In these three cases, it will be shown how the multiple scattering or multiple reflections along the medium boundaries significantly increase the apparent aperture of the TRM, and how this acts on the resulting focal spot size and on the quality of the spatiotemporal compression.

1.4. Comparison between TRMs and phase-conjugated mirrors

The basic principle of a TRM is an extension of an optical phase-conjugated mirror (PCM). If $P(r, \omega)$ is the temporal Fourier transform of $p(r, t)$, then the temporal Fourier transform of $p(r, -t)$ is $P^*(r, \omega)$. Therefore, the TR of pulsed signals is mathematically equivalent to the phase conjugation of monochromatic waves. However, there are some fundamental differences between these two techniques.

Since the time responses of detectors are very long compared with the period of optical waves, an optical PCM relies on nonlinear effects in the bulk of some medium to measure and to conjugate the phase information on monochromatic wavefields [9, 10]. Information on the amplitude and phase distribution of the signal wave can be recorded during its nonlinear interaction with one or two pump waves. In the three-wave mixing technique (two input waves, one output) one planar pump wave E_1 at frequency 2ω and the signal wave E at frequency ω interact in a quadratic nonlinear medium to give an output field E_c at frequency ω that is the conjugate of the signal wave. The mixing is efficient if strict phase matching conditions are satisfied by the different wavevectors. This limits the interest of the technique in optics to signals that are nearly collinear with the pump wave, imposing severe limitations upon input acceptance angle and focusing capability.

The most popular technique in optics is four-wave mixing (FWM). It requires a cubic nonlinearity in the interaction medium. It involves the incidence of three input waves of the same frequency (two planar counterpropagating pump waves E_1 and E_2 with wavevectors k_1 and k_2 and the wave E to be conjugated) with the generation (through the cubic nonlinearity) of an output field proportional to E_c the complex conjugate of E. Because $k_1 + k_2 = 0$ the phase matching condition is satisfied for all input angles of the signal and hence FWM can phase-conjugate an arbitrary wavefield. FWM can be understood as a real-time dynamic holographic method. Using the grating point of view in holography, the phase-conjugation process can be represented as a simultaneous recording and reading of two sets of gratings. The first grating is produced by the interference between the signal wave E and the pump wave E_2. The phase conjugated wave is produced by Bragg diffraction of E_1 from this grating. At the same time, another component of the phase conjugated wave is generated by Bragg diffraction of pump wave E_2 from another grating produced by the interference of E with E_1. The total radiated conjugate field is due to the coherent superposition of both processes.

1.5. Ultrasonic phase conjugated mirrors

Different authors have developed ultrasonic PCMs based on the use of monochromatic signals and nonlinear effects.

Initially, as in optics, FWM mechanisms based on cubic nonlinearity of an acoustic medium were considered. But in liquid the cubic nonlinearity is very weak compared with the quadratic nonlinearity (the ratio of the two coefficients is proportional to M^2, where M is the Mach number, usually $<10^{-3}$). To enhance the cubic nonlinearity, the use of liquids containing air bubbles [11, 12], small particles [13] and thermoacoustic nonlinearity [14] has been suggested. The holographic mechanism of phase conjugation was observed in these cases, with relatively weak efficiency, $<5\%$. Three-wave mixing has also been observed in liquid containing bubbles or polymer microparticles flickering at a frequency twice the acoustic frequency [15].

However the main limitation of the use of hydrodynamic nonlinearity arises from the fact that, contrary to the optical case, there is no dispersion in acoustics and the standard phase matching conditions $\omega_1 + \omega_2 = \omega_3$, $\boldsymbol{k}_1 + \boldsymbol{k}_2 = \boldsymbol{k}_3$ are always verified. When

the pump wave amplitude is increased in order to produce noticeable phase conjugation, a cascade of harmonics appears resulting in a periodic shock wave and in strong dissipation, and very complicated situations arise because of the resonant interactions of higher harmonics. This effect is typical of acoustics and is not observed in optics where the phase matching condition is very difficult to obtain and only works for well defined frequencies and geometries.

Another approach of phase conjugation is to generate phase conjugate sound waves in a solid. In these techniques, the acoustic pump wave is replaced by an electromagnetic pump wave that modulates the sound velocity of a nonlinear piezoelectric or magnetostrictive medium. Recently these techniques have proven to be significantly more efficient than FWM. However, they were first discussed in solid state physics more than 30 years ago [16,17] mainly with the terminology of phonon echoes.

The way to produce large phase conjugate sound waves in a solid is to use the uniform modulation of the sound velocity by an alternating electromagnetic field oscillating with a frequency twice that of the incident radiation. The difference between the velocities of acoustic and electromagnetic waves by five orders of magnitude allows one to produce the electromagnetic pump almost uniformly distributed in a region that covers a great number of sound wavelengths. Piezoelectric or ferromagnetic media can be used to process the nonlinear mixing. In all these techniques the sound velocity in the solid medium may be written as $c = c_0(1 + \Delta_c/c_0 \cdot \sin(2\omega t))$. When an incoming signal wave at frequency ω propagates along such a medium a parametric mechanism produces a backward phase conjugate wave at frequency ω. The coupling equation has been studied by Nelson [18]. He found that the ratio of the amplitude of the phase conjugate wave to that of the normal incident wave at the entrance of the interaction region is equal to

$$K = \tan(\Delta c/c_0 kL) \tag{9}$$

where k is the wavevector in the solid, L the thickness of the parametric interaction zone and $\Delta c/c_0$ is the sound velocity modulation.

Ohno [19–21] has extensively studied a similar effect in nonlinear piezoelectric-like $LiNbO_3$ crystal and PZT ceramics. He shows recently on PZT samples an efficiency K of nearly 25% at 10 Mhz.

Higher efficiency was experimentally observed by Brysev in magnetostrictive ceramics based on nickel ferrite [22,23] by mixing the incident wavefront with an oscillating magnetic field that modulates the sound velocity in the ferrite. The interest of this technique is that K is extremely high. Amplification of the phase conjugate wave by factors greater than 10 dB has been observed by Bryzev *et al* [24].

Another interesting parametric technique has been developed by Nikoonahad and Pusateri [25]. The PCM is based, as in the TRM approach, on a transducer array that samples an incident monochromatic wavefront. The signals collected from each array element are electronically mixed with a second-harmonic signal, using an array of mixers. The difference frequency signal so obtained has a phase that is the conjugate of that of the incident wavefront. The transducer array then retransmits the conjugated signals. One limitation of the technique is the continuous wave mode operation. Also, in principle, the phase-reversed signals have to be fed back to the same array element at which the wavefront was sampled and this results in a short-circuit across the two ports of the mixer. To overcome this difficulty, Nikoonahad feeds the conjugated signals to the element immediately adjacent to where the wavefront was sampled. The transducer array is then made of two sets or interlaced elements: those that sample the wavefront and those that transmit the conjugated wavefront. In order to avoid phase shift due the spatial offset, the array pitch has to be $\lambda/4$.

To conclude on these various techniques of acoustic phase conjugation, the nonlinear piezoelectric and magnetostrictive techniques are very attractive. However, amplification of the phase conjugate wave is only obtained for very-narrowband waves containing some hundred oscillations and for long interaction thickness L, as shown in (10). Besides, the efficiency K of the phase conjugate process varies with the incidence angle, and the maximum acceptance angle obtained were limited to $\pm 10^{\circ}$. Such a severe limitation upon the input angle seriously limits the focusing capability of these techniques.

Another experimental limitation of phase conjugation into a solid medium is due to the impedance mismatch between fluid and solid. When the incident beam comes from a fluid (as in medical applications), both the classical reflected waves between the different fluid–solid interfaces and the backward phase conjugate wave are observed. These waves can interfere and it is often difficult to clearly separate them. With TRMs, the ability to retransmit the time-reversed wave at any time facilitates the applications of this technique for most purposes.

2. Time reversal experiments

2.1. The experimental setup

In this section, three examples of TR experiments conducted with TRMs are presented: the first in a medium with high-order multiple scattering, the second in a waveguide and the last one in a chaotic cavity.

The first two experiments use the same transducer array and the same multichannel apparatus, only the propagation medium differs. A pointlike ultrasonic source (a single transducer) transmits a short pulse (usually 2 or 3 cycles) that propagates through the medium. Opposite to the source is a TRM made of a linear array of 128 transducers, all of them identical to the source. The TRM receives a set of 128 signals, digitizes and records them into electronic memories. These digital signals are time reversed, converted into analogue signals and retransmitted by the mirror into the medium. Then the resulting signal is measured by the same transducer that was previously used as the source. This transducer can also be translated in the source plane, while the recorded time-reversed signals are transmitted several times, in order to measure the signal recreated around the source, which provides the directivity pattern of the time-reversed waves.

The array centre frequency is 3.5 MHz, with a 50% bandwidth (at -6 dB). Each transducer element has its own receiving amplifier, an 8 bit A/D converter working at a 20 MHz sampling rate and a storage memory. The emission uses an 8 bit D/A converter followed by a linear power amplifier. The transmitter delivers a 30 V peak-to-peak voltage to a 50 Ω transducer impedance. In the receive mode, a logarithmic amplifier allows the recording of a 90 dB instantaneous dynamic range through the 8 bit A/D converters. Exponentiation of the data is applied to each buffer memory to compensate for the logarithmic operation before TR. Since each element is independent from the others, the operator can choose which elements of the array will actually perform the TR operation, and thus vary the mirror's aperture. The prototype allows a complete TR operation in less than 1 ms. The transducer size is 0.38 mm and the array pitch 0.42 mm, so the maximum aperture of the TRM is 54 mm.

2.2. Time reversal in multiply scattering media

Derode *et al* [26] carried out the first experimental demonstration of the reversibility of a multiply scattered acoustic wave by means of a TRM. In particular, it was shown that TR focusing is a very robust method that can refocus a wave even in the presence of very-high-

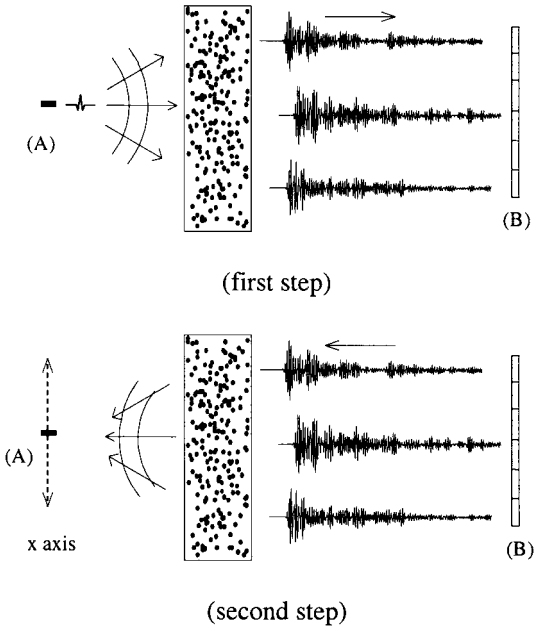

Figure 1. Experimental setup. In the first step the source (A) transmits a short pulse that propagates through the rods. The scattered waves are recorded on a 128-element array (B). In the second step, the 128 elements retransmit the time-reversed signals through the rods. The piezoelectric element (A) is now used as a detector. It can be translated along the x axis while the same time-reversed signals are transmitted by B, in order to measure the directivity pattern.

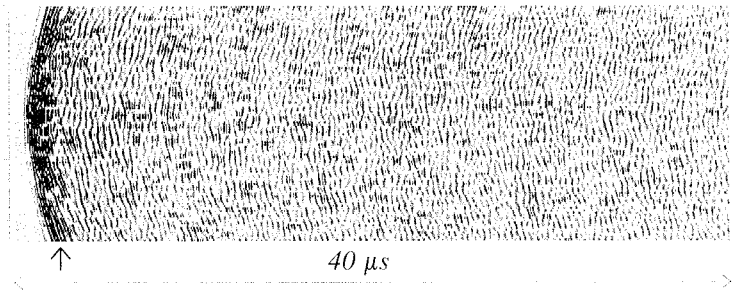

Figure 2. Signals received on a 128-element array. Time is the abscissa, and each line of the picture represents the signal received by one element. The arrow points to the ballistic front.

order multiple scattering. In an experiment such as the one depicted in figure 1, a multiple scattering sample is placed between the source and the array. The entire setup is in a water tank. The scattering medium consists of a set of hundreds of parallel steel rods (diameter 0.8 mm) randomly distributed. The sample thickness is $L = 15$ mm, and the average distance between rods is 2.3 mm. The source is 30 cm away from the TRM and transmits a short (1 μs) ultrasonic pulse (2.5 cycles of a 3.5 MHz sine wave). Figure 2 shows the set of signals received on the array: after the arrival of a first wavefront corresponding to the so-called ballistic wave, a long incoherent wavetrain is observed, which results from the multiply-scattered contribution. It corresponds to the multiple reflection of the initial pulse along all possible paths between the scatterers. The intensity of the ballistic front decays exponentially with the sample thickness L. The decay length is the mean free path, and multiple scattering dominates when L is significantly larger than one. In this sample, the mean free path was found to be of the order of 4 mm. Figure 3(a) shows the signal received at one particular element of the array. Note that it spreads over more than 80 μs, i.e. $\sim$100 times the initial pulse duration.

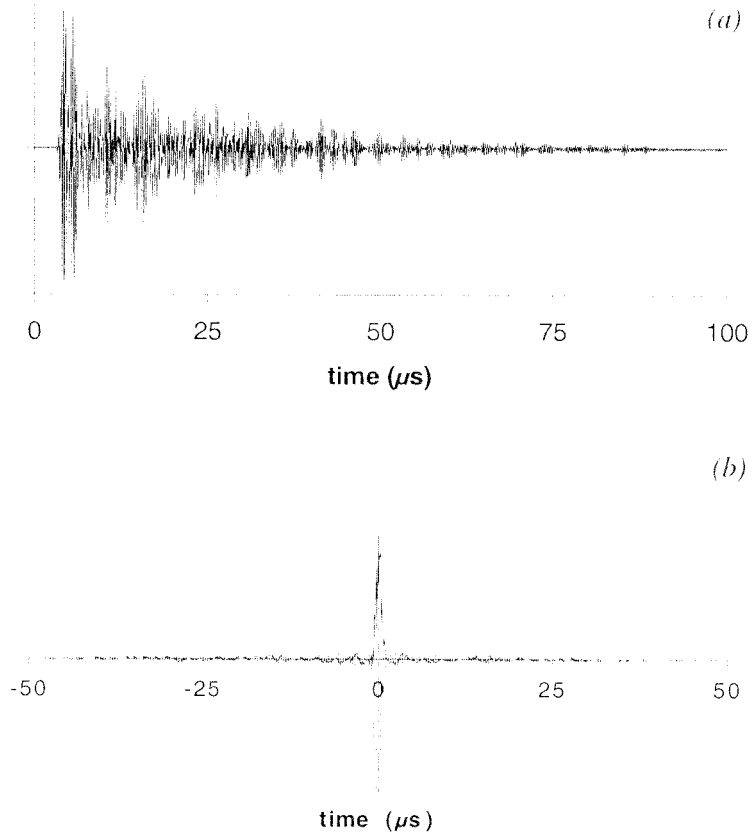

Figure 3. (*a*) Signal received on the TRM by one of the elements (the time origin is arbitrary). (*b*) Signal received on the source after time reversing the scattered signals.

2.2.1. Temporal compression and spatial focusing. In the second step of the experiment, the scattered signals are time reversed and a hydrophone measures the time-reversed wave around the source location. Two different aspects of this problem have been studied: the signal recreated at the source location (time compression) and the spatial distribution of the time-reversed wave around the source location (spatial focusing).

First, the time-reversed wave traverses the rods back to the source, and the signal received on the source is represented in figure 3(*b*): an impressive compression is observed, since the received signal lasts about 1 μs, against over 100 μs for the scattered signals.

Secondly, the pressure field is measured around the source, in order to get the directivity pattern of the beam emerging from the rods after TR. The results are plotted in figure 4 and an astonishing resolution is observed. Multiple scattering has *not* degraded the resolution of the system: indeed, in this particular case, the resolution is found to be six times finer than the classical diffraction limit!

This effect does not contradict the laws of diffraction, though. The intersection of the incoming wavefront with the sample has a typical size D. After TR, the waves travel on the same scattering paths and focus back on the source as if they were passing through a converging lens with size D. The angular aperture of this pseudo-lens is much wider than that of the array alone, leading to an improvement in resolution. In other words, because of

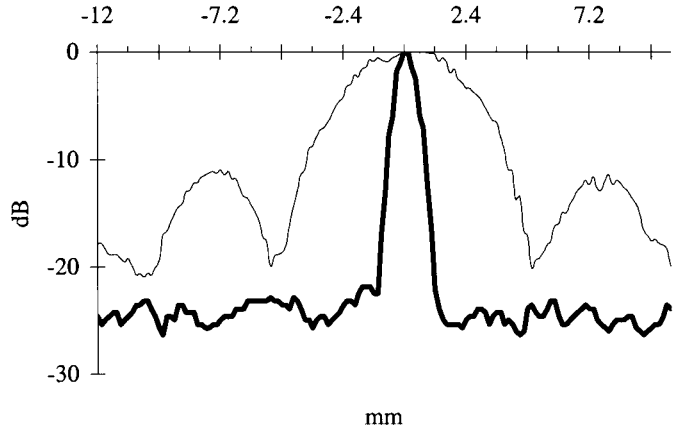

Figure 4. Directivity patterns of the TRM through the rods (thick curve) and without the rods (thin curve).

the scattering sample, the array is able to detect higher spatial frequencies than in a purely homogeneous medium. High spatial frequencies that would have been lost otherwise are redirected towards the array, due to the presence of the scatterers in a large area. Thus, multiple scattering coupled with a TRM is an efficient way of artificially increasing the aperture of the system.

2.2.2. Robustness of the time reversal process. These experimental results indicate that the time-reversed waves actually seem to be able to go backwards following the same intricate paths and find their way back to the source. This is indeed surprising.

In past years, TR experiments involving particles moving like balls on an elastic billiard table have been simulated numerically [27]. Even though each collision is theoretically a time-reversible process, making a group of balls travel back to its original state appears to be impossible. This apparent irreversibility originates from the high sensitivity to initial conditions, which is a typical property of nonlinear chaotic systems. When one tries to reverse the motion of the system, the slightest error increases dramatically with time. Since it is impossible to achieve an infinite accuracy, the system is irreversible over distances larger than the mean free path. Yet, the acoustic TRM seems to contradict these results. What is the origin of this robustness?

The wave or particle nature of the problem is a key element to the robustness of a TR device. Recently, Snieder and Scales [27] have performed numerical simulations to point out the fundamental difference between waves and particles in the presence of multiple scattering by random scatterers. In fact, they used TR as a diagnostic of wave and particle chaos: in a TR experiment, a complete focusing on the source will only take place if the velocity and positions are known exactly. The degree to which errors in these quantities destroy the quality of focusing is a diagnostic of the stability of the wave or particle propagation. Intuitively, the consequences of a slight deviation in the trajectory of a billiard ball will become more and more obvious as time goes on, and as the ball undergoes more and more collisions. Waves are much less sensitive than particles to initial conditions. Precisely, in a multiple scattering situation, the critical length scale that causes a significative deviation at a time t in the future decreases exponentially with time in the case of particles, whereas it only decreases as the square root of time for waves in the same situation.

The classical equivalent of a wave problem can be obtained by making the wavelength tend to zero (or, in the case of quantum mechanics, by letting Planck's constant go to zero). In a real experiment such as the one presented above, the wavelength is not zero and has to be compared with the typical scales of the system. In the disordered samples studied by Derode *et al*, the characteristic distances were of the same order as the average wavelength (0.45 mm): hence it is clearly a wave problem, and not a particle problem.

Waves and particles react in fundamentally different ways to perturbations of the initial conditions. The physical reason for this is that each particle follows a well defined trajectory whereas waves travel along all possible trajectories, visiting all the scatterers in all possible combinations. While a small error in the initial velocity or position makes the particle miss one obstacle and completely changes its future trajectory, the wave amplitude is much more stable because it results from the interference of all the possible trajectories and thus small errors in the transducer operations will sum linearly resulting in a small perturbation.

As any linear and time-invariant process, wave propagation through a multiple scattering medium may be described as a linear system with a certain impulse response. If the source sends a Dirac pulse $\delta(t)$, the jth transducer of the TRM will receive a signal $h_j(t)$ ($h_j(t)$ is the propagation impulse response from the source to transducer j). Moreover, due to spatial reciprocity, $h_j(t)$ is also the impulse response describing the propagation of a pulse from the jth transducer to the source. Thus, if the transducer is able to record and time reverse the whole impulse response, the signal generated at the source is given by the convolution $h_j(t) * h_j(-t)$.

This convolution product, in terms of signal analysis, is typical of a *matched filter*. Given a signal as input, a matched filter is a linear filter whose output is optimal in some sense. Whatever the impulse response $h_j(t)$, the convolution $h_j(t) * h_j(-t)$ is maximal at time $t = 0$. This maximum is always positive and equals $\int h_j^2(t)\,\mathrm{d}t$, i.e. the energy conveyed by $h_j(t)$. This has an important consequence. Indeed, with an N-element array, the signal recreated on the source can be written as a sum

$$s(t) = \sum_{j=1}^{j=N} h_j(t) * h_j(-t). \tag{10}$$

Even if the $h_j(t)$ are completely random and apparently uncorrelated signals, each term in this sum reaches its maximum at time $t = 0$. So all contributions add constructively around $t = 0$, whereas at earlier or later times uncorrelated contributions tend to interfere destructively one with another. Thus the recreation of a sharp peak after TR on a N-element array can be viewed as an interference process between the N outputs of N matched filters.

The robustness of the TRM can also be accounted for through the matched filter approach. If for some reason, the TRM does not exactly retransmit $h_j(-t)$ but rather $h_j(-t) + n_j(t)$, where $n_j(t)$ is an additional noise on channel j, then the recreated signal is written:

$$\sum_{j=1}^{j=N} h_j(t) * h_j(-t) + \sum_{j=1}^{j=N} h_j(t) * n_j(t).$$

The time-reversed signals $h_j(-t)$ are tailored to exactly match the medium impulse response, resulting in a sharp peak. A small additional noise, however, is not matched to the medium and given the length of the re-broadcast signal (100 times that of the initial pulse), generates a low-level long-lasting background noise instead of a sharp peak.

2.2.3. Theoretical analysis of reversibility in random media. To go further with this approach, a simple theoretical model based on impulse responses has been developed [28]. A deterministic model would have to take into account the exact position of each rod, which

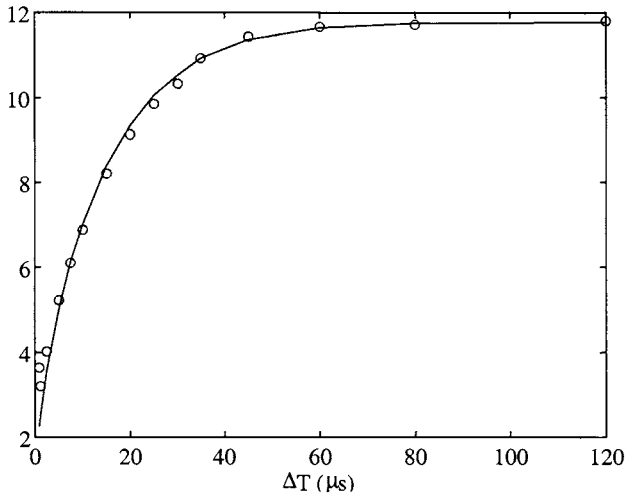

Figure 5. TR with one array element through a 15 mm thick scattering sample: peak-to-noise ratio ϑ versus duration of the TR window. The circles are the experimental results, the solid curve represents the theoretical prediction based on a shot noise model.

is infeasible. Instead, the rods can be considered randomly and uniformly distributed. Such a model can only investigate *average* quantities such as the mean value and variance of the recreated signal as a function of relevant parameters.

In [28] Derode has considered a simple model in which the impulse response $h_j(t)$ is treated as shot noise modulated by a slowly varying envelope, i.e. a series of replicas of the initial impulse, arriving at random and uncorrelated times:

$$h_j(t) = E(t) \sum_i a(t - t_i). \tag{11}$$

Here, the t_i are random arrival times corresponding to all possible scattering path lengths within the sample, $a(t)$ represents the acoustoelectrical response of the transducers and $E(t)$ is a deterministic envelope function that take into account the slow decay of the signal. In a regime of strong multiple scattering, $E(t)$ can be well represented by a solution of the diffusion equation.

For relatively thin samples ($L = 15$ mm, with a mean free path of 4 mm), the predictions of this model were found to be in excellent agreement with the experimental results (see figure 5). The quality of time compression was assessed by a parameter ϑ, defined as the ratio of the peak amplitude to the surrounding noise:

$$\vartheta = \frac{\max\{s(t)\}}{\sqrt{\int s^2(t)\,\mathrm{d}t}} \tag{12}$$

where the integral is taken over a time interval excluding the peak. Figure 5 compares experimental measurements of ϑ with theoretical prediction based on a 'shot noise' approach, which is apparently very accurate. However, it should be noted that a 'shot noise' model, based on the assumption that the arrival times t_i correspond to independent paths, is too simple for very thick samples. When the sample thickness increases, the probability of crossing paths increases too, inducing a correlation in the arrival times.

Time reversal as a temporal correlator. $h_j(t)$ being a random signal, the quality of TR strongly depends on the statistical parameters of the impulse response, particularly its autocorrelation function $\langle h_j(t_1)h_j(t_2)\rangle$, where the brackets $\langle\ \rangle$ denote an ensemble average.

For instance, in the case of the 'shot noise' approach, the autocorrelation function is

$$\langle h_j(t_1)h_j(t_2)\rangle = E(t_1)E(t_2)R_a(t_1 - t_2) \tag{13}$$

with $R_a(t)$ the autocorrelation function of $a(t)$. This means that the correlation time τ_c of the transmitted signal is roughly twice the duration of the acoustoelectrical response and is inversely proportional to the frequency bandwidth.

Carrying out a TR experiment consists in recording the scattered signal within a time window $[T_1, T_2]$ and sending the time-reversed signal back through the rods. Due to reciprocity, the inward and outward propagation impulse responses are the same. Hence, the signal recreated on the source after time reversing on the jth element writes:

$$s_j(t) = \int_{T_1}^{T_2} h_j(\theta)h_j(t+\theta)\,\mathrm{d}\theta. \tag{14}$$

This signal is also random, and is likely to fluctuate from one realization to the other. But we can calculate its statistical average:

$$\langle s_j(t)\rangle = \int_{T_1}^{T_2} \langle h_j(\theta)h_j(t+\theta)\rangle\,\mathrm{d}\theta.$$

If the shot noise approach is valid, we have

$$\langle s_j(t)\rangle = R_a(t)\int_{T_1}^{T_2} E^2(\theta)\,\mathrm{d}\theta. \tag{15}$$

These results call for several comments.

First, on average, the signal recreated at the source after TR is symmetrical and its duration is determined by τ_c, the correlation time of the scattered signal. Its amplitude increases if the TR window is wider.

Indeed, TR can be interpreted as a correlator: $s_j(t)$ can be viewed as an unbiased estimate of the correlation function $\langle h_j(t_1)h_j(t_2)\rangle$. How accurate (or, in statistical terms, *consistent*) this estimator will be, and how strongly the peak will arise from the noise, will depend on the variance of $s_j(t)$.

Since τ_c denotes the correlation time of the scattered signal, the ratio $(T_2 - T_1)/\tau_c$ gives the number of independent pieces of information (or 'information grains') within the TR window $[T_1, T_2]$. When the window is expanded, more and more new information (i.e. uncorrelated with previous data) are added, and the resulting enhancement of the peak-to-noise ratio is proportional to the square root of the number of so-called 'information grains'.

Actually, this would be true if all information grains had the same weight, i.e. if the envelope of the transmitted signal $E(t)$ were a constant. When this is not the case, the peak-to-noise ratio can be predicted by a more complicated formula, taking into account $E(t)$. As is shown in figure 5, the theoretical prediction nicely fits the experimental results.

So far, in the theoretical analysis, only one element was performing the TR operation. In fact, contributions from all active elements on the array have to be taken into account. Thus, for a N-element array, the signal recreated on the source after TR is a sum of N random contributions

$$s(t) = \sum_{j=1}^{N} s_j(t).$$

All contributions add constructively at time $t = 0$ to form the central peak. Outside the peak, the question is whether the $s_i(t)$ and $s_j(t)$ are correlated or not. If they receive the same information, two array elements i and j will contribute to the total signal $s(t)$ in the same way, and adding these two contributions will not enhance the contrast. However, if they receive uncorrelated data, their contribution to the noise surrounding the peak will also be uncorrelated and will tend to destroy one another. Once more, the relevant parameter is the number of uncorrelated data (now as a function of space) available on the array, or so-called 'spatial information grains'.

As the number N of transducers is increased, the SNR should increase proportionally to the square root of 'information grains' intercepted by the array. The experimental values of the SNR observed as a function of N for $L = 15$ mm are in agreement with this idea. However, for larger thickness ($L \sim 80$ mm), a recent study (to be published) shows that long-range correlations complicate the interpretation of the experimental results.

Essentially, the best situation would be one in which all array elements receive totally independent information, as if the scattered wave were spatial white noise. However, this is not physically possible for two reasons. First, the ballistic front is identical on all array elements, and remains apparent despite the fact that the sample thickness is roughly four times the transport mean free path. Second, even in the multiple scattering contributions, the correlation length of the signals received on the array cannot be arbitrarily small. This is based on a fundamental theorem of statistical optics, the Van Cittert–Zernike theorem, which states that the wavefield generated by a fully incoherent random source has a typical correlation length $\lambda z/D$, D denoting the size of the random source and z the propagation distance. Here the multiple scattering *halo* just emerging from the sample can be seen as a random source. As the distance z between the sample and the receiver increases, the correlation length increases too. A physical interpretation of the Van Cittert–Zernike theorem is that propagation in water smooths the rugged wavefronts emerging from the sample. In theory, one way to improve the efficiency of a TRM would be to put the transducers as close to the sample as possible. In practice, this is difficult because of back-and-forth reflections between the transducers and the scattering sample.

Time reversal as a spatial correlator. The number of spatial 'information grains' available on the array is crucial not only to the peak-to-noise ratio, but also to the spatial resolution of the system. As an example, figure 6 shows two directivity patterns. They have been obtained after time reversing 2 μs of the transmitted signals either at early times (i.e. including the ballistic front), or 20 μs later. At early times the -6 dB resolution is 6.3 mm, as in a homogeneous medium, whereas at later times the resolution drops to 0.6 mm!

The physical interpretation of this phenomenon is simple. The ballistic front is what is left from the incoming wave, i.e. it corresponds to rays that go straight from the source to the array, as in a homogeneous medium, whereas later arrivals correspond to multiple scattering contribution and contain higher spatial frequencies. During the backpropagation, the medium plays the role of a lens focusing the wave back on the source. At early times (as in a homogeneous medium) the angular aperture of the pseudo-lens is that of the array alone, whereas at later times its angular aperture is widened by scattering, which accounts for the dramatic increase in resolution.

Another way to consider the spatial resolution of the system is to follow the impulse response approach and treat the TR process as a spatial correlator. If we note $h'_j(t)$ the propagation impulse response from the jth element of the array to an observation point O

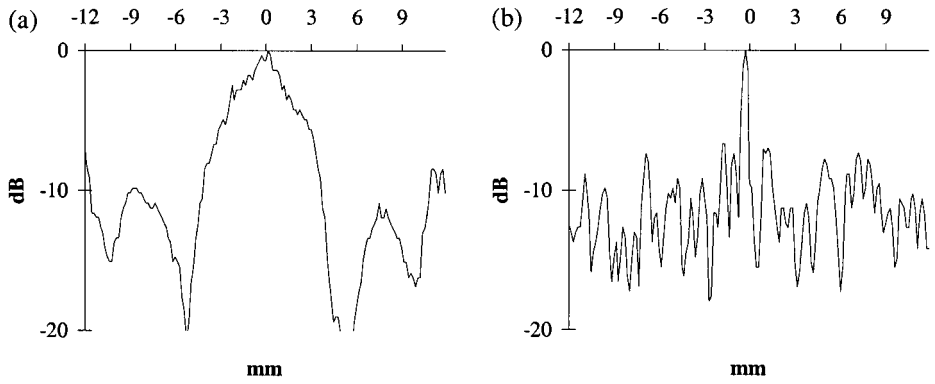

Figure 6. Directivity patterns of the time-reversed waves around the source for a 2 μs time window picked in the scattered signals (*a*) at early times and (*b*) at later times.

different from the source S, the signal recreated in O at time $t = 0$ is

$$\int h_j(\theta)h'_j(\theta)\,\mathrm{d}\theta. \tag{16}$$

Note that this expression can be used as a way to define the directivity pattern of the time-reversed waves around the source. Now, due to reciprocity, the source S and the receiver can be exchanged, i.e. $h'_j(t)$ is also the signal that would be received in O if the source was the jth element of the array. Therefore, we can imagine this array element is the source, and the transmitted field is observed at two points O and S. The spatial correlation function of this wavefield would be

$$\langle h_j(t)h'_j(t)\rangle$$

and equation (16) can be viewed as an estimator of this spatial correlation function.

In that sense, the spatial resolution of the system (i.e. the -6 dB width of the directivity pattern) is simply an estimate of the *correlation length* of the scattered wavefield, in the same way that the duration of the signal refocused on the source could be viewed as an estimate of the correlation time of the scattered signal.

As can be seen in figure 2, the coherence length is larger at early times (since the ballistic front is almost identical on all elements of the array) than in the multiple scattering regime, which is another way to account for the increase in resolution at later times.

The finest resolution should be obtained by time reversing the last part of the transmitted signals. However, since the amplitude of the transmitted signals decreases with time, the later time contributions have relatively small amplitudes and are more sensitive to noise, which generates a higher side-lobe level. A trade-off has to be found between the resolution enhancement and the side-lobe level. The directivity pattern displayed in figure 4 is an example of this trade-off: the resolution is 1.05 mm, six times thinner than in a homogeneous medium, with a side-lobe level as low as -24 dB.

Finally, the fundamental properties of TR in a random medium rely on the fact that it is a space and time correlator, and the time-reversed waves can be viewed as an estimate of the space and time autocorrelation functions of the waves scattered by a random medium. The quality of TR is the same as that of a statistical estimate: the estimate is better if it is built from a larger amount of uncorrelated information.

Moreover, the system is not sensitive to a small perturbation since adding a small noise to the scattered signals (e.g. by digitizing them on a reduced number of bits) may alter the

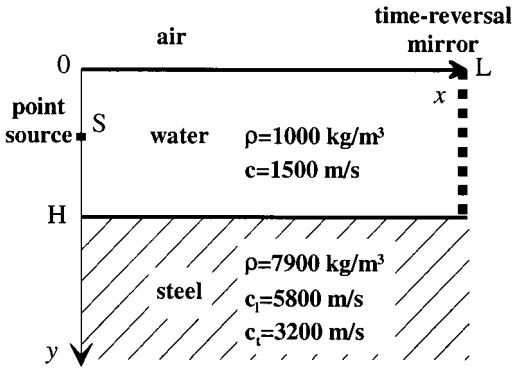

Figure 7. Schematic diagram of the acoustic waveguide: the guide length ranges from 40 to 80 cm and the water depth from 1 to 5 cm. The central acoustic wavelength (λ) is 0.5 mm. The array element spacing is 0.42 mm. The TRM is always centred at the middle of the water depth.

noise level but does not drastically change the correlation time or the correlation length of the scattered waves. Even in the extreme case where the scattered signals are digitized on a single bit, Derode has shown [29] that the time and space resolution of the TRM were practically unchanged, which is striking evidence for the robustness of wave TR in a random medium.

2.3. Time reversal in waveguides

In the TRC approach, the array of transducers samples a closed surface surrounding the acoustic source. In the last section, we have seen how the large length of paths involved in the multiple scattering experiment widens the effective TRM aperture. The same effect may be obtained for waves propagating in a waveguide. Indeed, multiple reflections on the guide interfaces significantly increase the apparent aperture of the TRM. The basic idea is to replace one part of the TRC transducers by reflecting boundaries that redirect the incident wave towards the TRM aperture. Thus, spatial information is converted into the time domain and the quality of the reversibility experiment depends crucially on the duration of the TR window, i.e. the length of the signal to be time reversed. As for a multiply scattering medium, acoustic propagation in a waveguide leads to the apparition of multiple replicas of the initial pulse. The main difference between a random multiscattering medium and a waveguide is that the arrival time of each wavefront in a waveguide is easily predictable and depends only on a few parameters such as the length and the depth of the guide. TR experiments in a waveguide make evident a temporal compression which is comparable to the one observed through a multiscattering medium and can be interpreted through the matched-filter approach introduced in section 2.2.2. On the other hand, the spatial focusing is interpreted by the method of images applied to the interfaces of the guide. A simple experiment conducted by Roux *et al* [30] demonstrates the spatial and temporal TR focusing with a small number of transducers in an ultrasonic waveguide.

2.3.1. Ultrasonic waveguide. The experiment is conducted in a waveguide whose interfaces (one water–air and one water–steel interface) are plane and parallel. The length of the guide is $L \sim 800$ mm along the y axis, which is of the order of 20 times the water depth $H \sim 40$ mm along the x axis. The medium is invariant under any translation along the z axis (figure 7). This permits restriction to a 2D analysis in the xy plane.

A pointlike ultrasonic source is located on one side of the waveguide. On the other side, a TRM, identical to the one used in the multiscattering medium, is used (see section 2.2.1); 96 of the array elements are used, which corresponds to an array aperture equal to the waveguide aperture. Then, each TR experiment is performed as previously described: (1) the point source emits a pulsed wave, (2) the TRM receives, time reverses and retransmits the field which

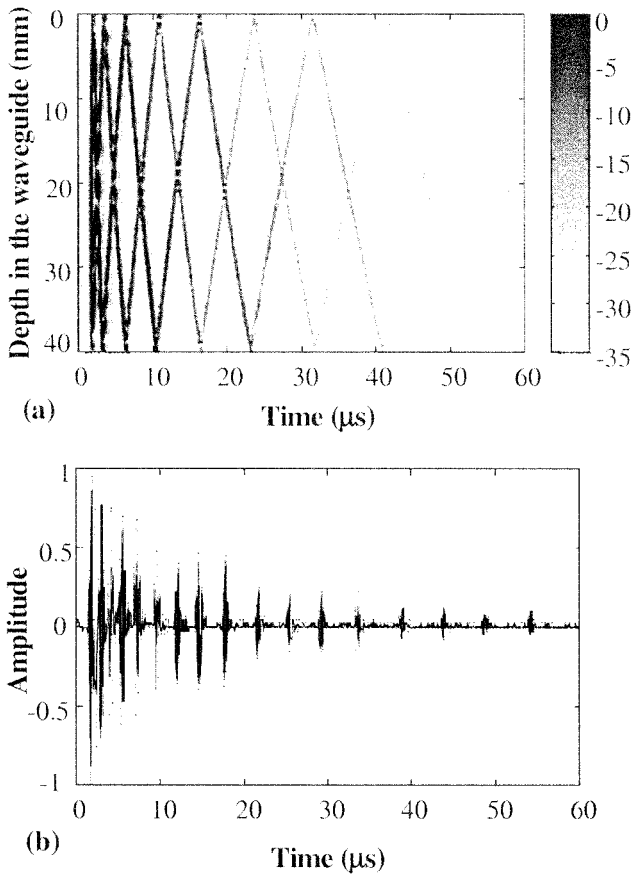

Figure 8. (*a*) Spatiotemporal representation of the incident acoustic field received by the TRM after propagation through the guide; $H = 40$ mm; $L = 74$ cm; source depth $= 20$ mm, (*b*) Temporal signal measured on one transducer of the array.

has propagated from the source through the waveguide, (3) after backpropagation, the time-reversed field is detected in the plane of the source. After the analysis of the incident wavefield received on the TRM, two aspects of the time-reversed field are studied: time compression at the source and spatial resolution around the source.

Figure 8(*a*) shows the field recorded by the TRM after propagation through the channel. After the arrival of the first wavefront corresponding to the direct path we observe a set of signals, due to multiple reflections of the incident wave between the interfaces, that spread over 100 μs. Figure 8(*b*) represents the signal received on one transducer of the TRM. After the TR of the 100 μs, we observe the spatiotemporal distribution of the time-reversed field on the source plane (figure 9(*a*)) and we note a remarkable temporal compression at the source location (figure 9(*b*)). This means that multipath effects are fully compensated. The signal observed at the source is nearly identical to the one received in a time-reversed experiment conducted in free space.

In this experiment, the transfer function of the waveguide has been completely compensated by the TR process. As with a multiple scattering medium, the TR process enables the realization of an optimal matched filter of the waveguide transfer function. The

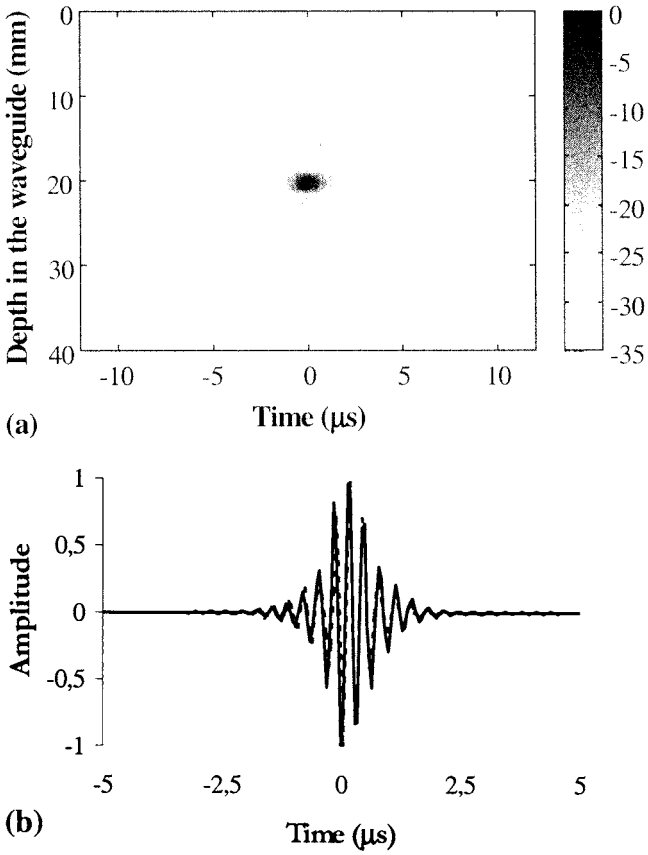

Figure 9. (*a*) Spatiotemporal representation of the time-reversed field measured in the plane of the point source: $L = 74$ cm; $H = 40$ mm; source depth $= 20$ mm; a 96-transducer TRM, (*b*) solid curve: zoom of the time-reversed signal measured at the point source between -5 μs and $+5$ μs (receiver depth $= 20$ mm); dashed curve: time-reversed signal measured at the source in free space.

analysis of figure 9 shows that the ratio between the peak signal and the side-lobe level is of the order of 45 dB.

The second part of the analysis of this TR experiment concerns the spatial focusing. Figure 10 shows the directivity pattern of the time-reversed field observed in the source plane. The time-reversed field is focused on a spot which is much smaller than the one obtained with the same TRM in free space. In our experiment, the -6 dB lateral resolution is improved by a factor of 9. This can be easily interpreted by the images theorem in a medium bounded by two mirrors. For an observer, located at the source point, the 40 mm TRM appears to be accompanied by a set of virtual images related to multipath reverberation. The effective TRM is then a set of TRMs as shown in figure 11. When taking into account the first ten arrivals, the theoretical effective aperture of the mirror array is ten times larger than the real aperture. However, in practice, as the replicas arrive later, their amplitudes decrease. The angular directivity of the transducers leads to an apodization of the effective aperture of the TRM. Figure 12 shows the effect of the time-reversed window duration on the width of the focal spot. The size of the focal spot increases when the number of replicas selected by the window

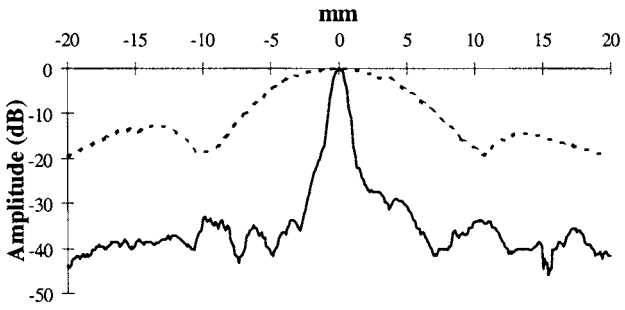

Figure 10. Directivity patterns of the time-reversed field in the plane of source: the dashed curve corresponds to free space, the solid curve to the waveguide; $H = 40$ mm; $L = 74$ cm; a 96-transducer TRM; source depth = 20 mm.

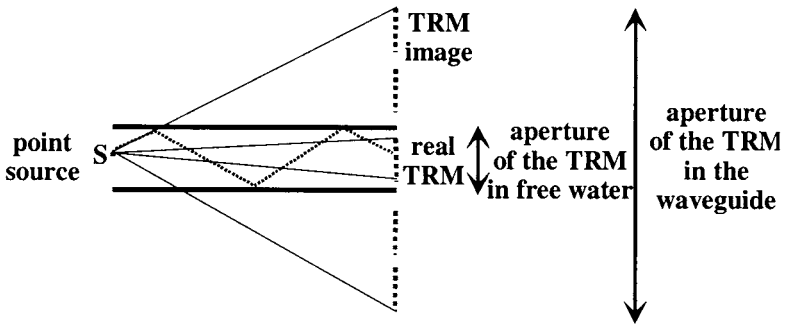

Figure 11. The principle of mirror images applied to the waveguide.

decreases. This clearly shows that the effective aperture of the TRM is directly related to the TR window duration. The -6 dB beamwidth is given by $\Delta \approx \frac{\lambda f}{A'}$ where A' is the effective aperture of the TRM: when all the replica are selected, we measure $A' = 9A$ where A is the array aperture.

2.3.2. Application of TR processing in underwater acoustics. Acoustic waveguides are currently found in underwater acoustics, especially in shallow water, where multipath propagation limits the capacity of underwater communication systems. The problem arises because acoustic transmission in shallow water bounces off the ocean surface and floor, so that a transmitted pulse gives rise to multiple arrivals on the receiver.

To compensate acoustic reverberation in the ocean, one-channel TR was first introduced in the early 1960s by Parvulescu and Clay [31, 32]. They performed experiments in shallow water at sea with one transducer working in a time-reversed mode. They observed temporal compression but their experiments did not embody the spatial focusing property of TRMs. Parvulescu's approach consists of considering the ocean as a correlator as written in 2.2.3. In 1991, Jackson and Dowling [4] developed a theoretical formalism to describe phase conjugation in the ocean. This formalism is based on the modal decomposition of the pressure field in an acoustic waveguide. Following this approach, Feuillade and Clay [33] computed in 1992 numerical TR experiments in shallow water. Since 1996, Kuperman *et al* [34–36] have performed several underwater acoustics experiments in a 120 m deep ocean waveguide. At a frequency of 500 Hz or 3.5 kHz, they used a 24-element TRM to accomplish TR focusing and

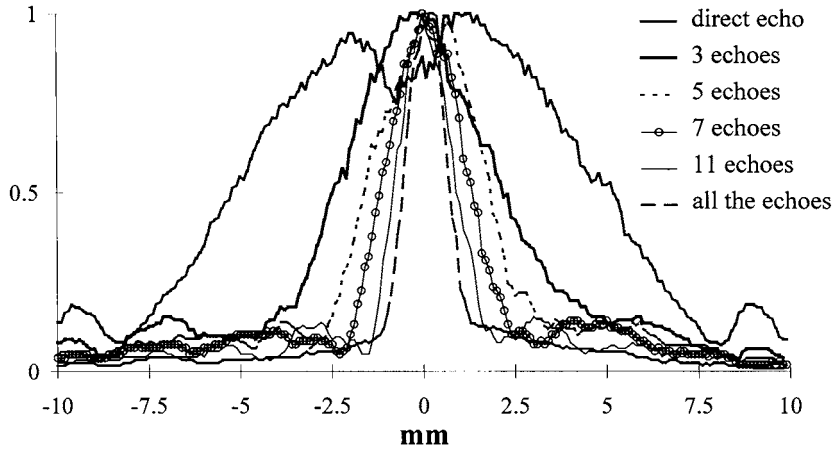

Figure 12. Directivity patterns (on a linear scale) of the time-reversed field versus the number of echoes selected in the time-reversed window; $H = 20$ mm; $L = 74$ cm; a 96-transducer TRM; source depth = 10 mm.

multipath compensation from 7 up to 30 km.

Theoretically speaking, for one spectral component at frequency ω, the TR operation consists of a phase conjugation of the incident field. For an incident field coming from a point source located at depth x_s, the phase conjugation, performed in shallow water, from a vertical array of N discrete sources leads to the time-reversed pressure field:

$$P(x, y, \omega) = \sum_{j=1}^{N} G_\omega(x, x_j, y) G_\omega^*(x_j, x_s, L) \tag{17}$$

where $G_\omega^*(x_j, x_s, L)$ is the conjugated monochromatic 'Green function' of the waveguide at frequency ω between a source at depth x_s and a receiver at depth x_j and range L. In other words, the phase-conjugated field in the plane of the source is the sum over the array elements of a product of two Green functions: one describes the propagation from the source to the array and the other describes the propagation from the array to the plane of the source. TR appears in the conjugation of the Green function between the source and the array in the right term of equation (17). In a range-independent waveguide, the Green function is expressed as

$$G_\omega(x, x_s, L) = \frac{\mathrm{i}}{\rho(x_s)(8\pi L)^{1/2}} \exp\left(-\mathrm{i}\frac{\pi}{4}\right) \sum_n \frac{u_n(x_s) u_n(x)}{k_n^{1/2}} \exp(\mathrm{i}k_n L) \tag{18}$$

where n is the number of propagating mode, $u_n(x)$ corresponds to the modal shape as a function of depth and k_n the wavenumber. To demonstrate that $P(x, y, \omega)$ focuses at the position of the initial source, we simply substitute (18) into (17) which specifies that we sum over all modes and array sources:

$$p(x, y, \omega) \approx \sum_j \sum_n \sum_m \frac{u_m(x) u_m(x_j) u_n(x_j) u_n(x_s)}{\rho(x_j)\rho(x_s)\sqrt{k_m k_n y L}} \exp(\mathrm{i}(k_m y - k_n L)). \tag{19}$$

For an array which substantially spans the water column, we appoximate the sum of sources as an integral and invoke the orthonormality of the modes:

$$\int_0^\infty \frac{u_m(x) u_n(x)}{\rho(x)} \, \mathrm{d}k = \delta_{nm}. \tag{20}$$

The sum over j selects mode $m = n$ and equation (19) becomes

$$P(x, y, \omega) \approx \sum_m \frac{u_m(x)u_m(x_s)}{\rho(x_s)k_m\sqrt{yL}} \exp(\mathrm{i}k_m(y - L)). \tag{21}$$

In the plane of the source at $y = L$, the closure relations which define the modes as a complete set ($\sum_m \frac{u_m(x)u_m(x_s)}{\rho(x_s)} = \delta(x - x_s)$) can be applied under the assumption that the k_n are nearly constant over the interval of the contributing modes. This leads to $P(x, L, \omega) \approx \delta(x - z_s)$, which proves that the phase-conjugated field focuses back at the source.

Kuperman *et al* have experimentally demonstrated in the ocean the robustness of TR focusing provided the array adequately samples the field in the water column. They have shown that temporal changes in the ocean due to surface waves and internal waves degrade the focus but that this degradation is tolerable if the average Green function is not severely perturbed by these time variations [34]. Moreover they experimentally achieved a shift of the focal range on the order of 10% by shifting the central frequency of the TRM prior to retransmission [35].

2.4. Time reversal in chaotic cavities

In this section, we are interested in another aspect of multiply reflected waves: waves confined in closed reflecting cavities such as elastic waves propagating in a silicon wafer. With such boundary conditions, no information can escape from the system and a reverberant acoustic field is created. If, moreover, the cavity shows ergodic properties and negligible absorption, one may hope to collect all information at only one point. Draeger *et al* [37–39] have shown experimentally and theoretically that in this particular case a TR can be obtained *using only one TR channel* operating in a closed cavity. The field is measured at one point over a long period of time and the time-reversed signal is re-emitted at the same position.

The experiment has been carried out by using elastic waves propagating in a monocrystalline silicon wafer. The material was chosen for its weak absorption. In fact, the decay periods of 10 to 20 ms are much greater than the largest TR windows used (1.5 ms) so that the mean intensity level inside can be considered constant. The wafers used are discs of thickness 525 μm and diameter between 100 and 125 mm, with a segment of variable size cut off. There are several modes of propagation possible (SH and two others corresponding to the S_0 and A_0 Lamb modes), propagation is dispersive and anisotropic. But the observed phenomena can be described successfully without taking these facts into account. Wave speeds vary between 2000 and 8000 m s^{-1} and rays in the cavity encounter typically between 80 and 400 reflections during a TR experiment.

Elastic waves are injected by aluminium cones fixed to transverse transducers (figure 13). Their tip touches the wafer and, vibrating with a given polarization, excites the different propagation modes. In addition, they can act as measuring instruments for the same polarization. After excitation, their influence on the wafer is negligible. The experiment is a two-step process as described above. In the first step, one of the transducers, located at point A, transmits a short omnidirectional signal of duration 0.5 μs (central frequency 1 MHz) into the wafer. Another transducer, located at B, observes a very long chaotic signal, that results from multiple reflections of the incident pulse along the edges of the cavity, and which continue for more than 50 ms corresponding to some hundred reflections along the boundaries. Then, a portion of 2 ms of the signal is selected, time reversed and re-emitted by point B. As the time reversed wave is an A_0 Lamb wave that induces vertical displacements of the silicon surface, it can be observed using an optical interferometer that scans the surface around point A.

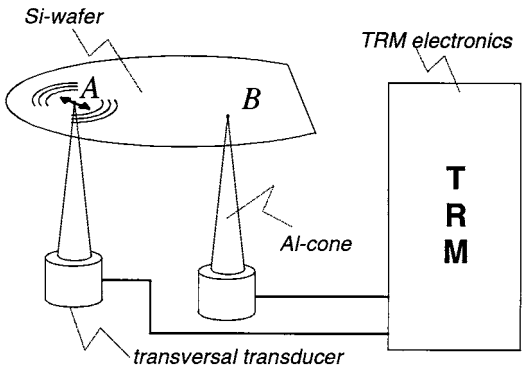

Figure 13. Experimental setup for the TR experiment conducted in a chaotic cavity.

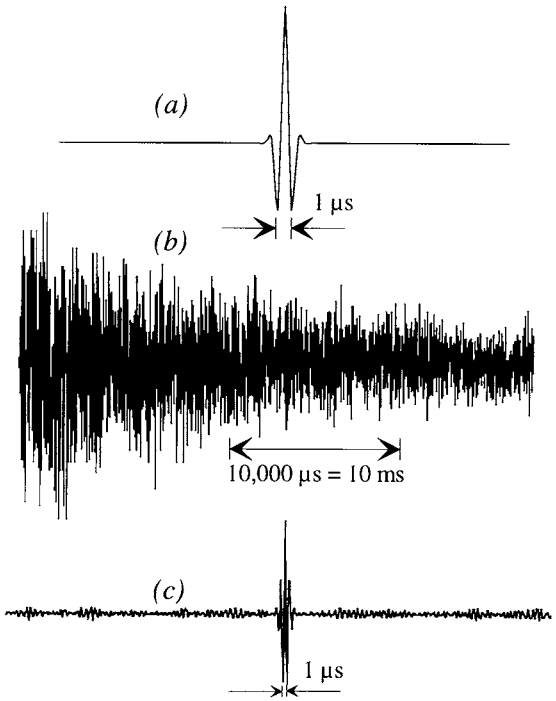

Figure 14. (*a*) Initially emitted signal by transducer A, (*b*) signal received at point B, (*c*) time-reversed signal observed at point A, with a TR window of $\Delta T = 1.5$ ms.

One observes both an impressive time recompression at point A and a refocusing of the time reversed wave around the origin (figures 14 and 15), with a focal spot whose radial dimension is equal to half the wavelength of the A_0 Lamb wave. Using reflections at the boundaries, the time-reversed wavefield converges towards the origin from all directions and gives a circular spot, like the one that could be obtained with a closed TRC covered with transducers. The 2 ms time-reversed waveform (that corresponds to nearly 2000 complicated oscillations) is the code needed to focus exactly on point A.

The success of this TR experiment is particularly interesting with respect to two aspects. Firstly, it proves the feasibility of TR in wave systems with chaotic ray dynamics. An equivalent

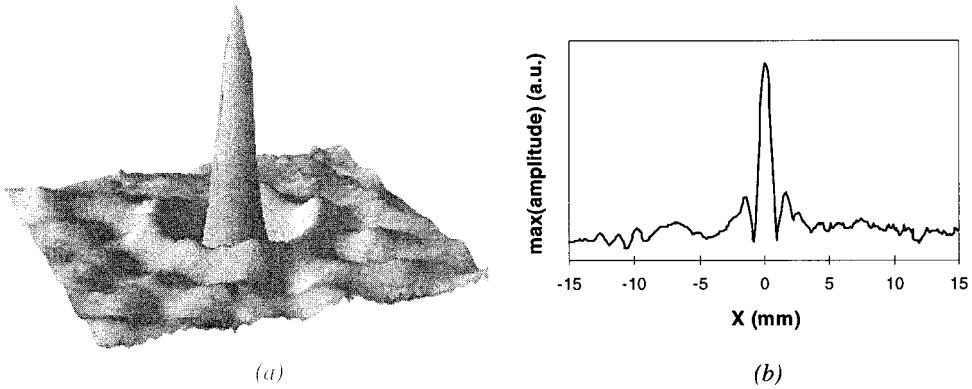

Figure 15. (*a*) Time-reversed wavefield observed on a square of 15 × 15 mm. (*b*) Close-up of the focal spot.

experiment would not be possible in the case of classical trajectories: despite the TR invariance of the governing equations, a TR would fail due to strong sensitivity to initial conditions. Paradoxically, in the case of one-channel TR, chaotic dynamics is not only harmless but even useful, as it guarantees ergodicity and mixing. Secondly, using a source of vanishing aperture, we obtain an almost perfect focusing quality. The procedure approaches the performance of a closed TRC which has an aperture of 360°. Hence, a one-point TR in a chaotic cavity produces better results than a TRM in an open system. Using reflections at the edge, focusing quality is not aperture limited, and in addition, the time-reversed collapsing wavefront approaches the focal spot from all directions.

Although one obtains excellent focusing, a one-channel TR is not perfect, as a weak noise level throughout the system can be observed. Residual temporal and spatial side-lobes persist even for TR windows of infinite size. They are due to multiple reflections passing over the locations of the TR transducers and they have been expressed in closed form by Draeger *et al* [39]. Using an eigenmode analysis of the wavefield, he shows that, for long TR windows, there is a saturation regime that limits the SNR. The reason is the following. By injection of a short pulse during the first step in A, the system acquires a certain eigenmode distribution. B records a long signal which can be interpreted as a superposition of all eigenfrequencies of the system. If the signal is sufficiently long and degeneracy is negligible (a condition presumably enhanced by the spectral rigidity of a chaotic wave 'billiard table'), these eigenfrequencies are well resolved. During the transmission of the time-reversed signal, every frequency excites then exclusively the corresponding eigenmode. To produce a perfectly reversed wavefield, every re-emitted eigenmode should have the same weight as during the first step of the experiment. However, B measures and injects each eigenmode with a factor proportional to the value of its eigenfunction at this point. In particular, the eigenmodes having a node in B cannot be measured at all. This confusion of the eigenmode weights is the origin of the information loss mentioned above. For the same reason, A cannot transmit in the cavity all the frequency components of a Dirac excitation. A is always located at the nodes of some eigenmodes and these eigenfrequencies cannot be transmit in the cavity.

More precisely, neglecting the acoustoelectric responses of the transducers and taking into account the modal decomposition of the impulse response $h_{AB}(t)$ on the eigenmodes $\psi_n(\vec{x})$

of the cavity (of eigenfrequency ω_n):

$$h_{AB}(t) = \sum_n \psi_n(A)\psi_n(B)\frac{\sin(\omega_n t)}{\omega_n} \qquad t > 0. \tag{22}$$

It has been shown that the time-reversed signal received at the initial source, i.e. the autocorrelation of the propagation impulse response $h_{AB}(t)$, cannot be simply reduced to a Dirac distribution $\delta(t)$, but is equal to

$$s(t) = h_{AB}(-t)^* h_{BA}(t) = h_{AA}(-t)^* h_{BB}(t) \tag{23}$$

where the impulse response $h_{AA}(t)(h_{BB}(t))$ describes backscattering properties of A (B) due to the boundaries of the cavity and are composed of a first peak during emission around $t = 0$ and some multiple reflections afterwards, which pass over the source point even after the excitation has ended. Indeed, the signal observed in A, the source location, after a Dirac excitation can be described by $h_{AA}(t)$. Therefore, a perfect TR operation (i.e. we simply count time backwards) would give in A the signal $h_{AA}(-t)$, i.e. some multiple reflections with a final peak around $t = 0$. Thus, multiple reflections passing over the source point are one of the reasons for temporal side-lobes. In the same way, the reversed point B cannot exactly transmitted any waveform in the cavity. Due to the boundaries, a Dirac excitation at B will also give rise to a transmitted signal $h_{BB}(t)$.

3. Acoustic time reversal in hydrodynamics

All of the previously discussed experiments show the focusing capability of TRMs in a static medium. TRM can also be used in hydrodynamics: in such media, violation of the symmetry is observed and the time-reversed field no longer focuses on its original source. A first example of this violation has been studied by Dowling [40]: he showed that a flow in uniform translation $\vec{U}(U/c \ll 1)$ induces irreversibility for acoustic propagation. Indeed, the monochromatic Green function $\mathbf{G}$ which describes acoustic propagation between $\vec{r}_a$ and $\vec{r}_b$ is

$$\mathbf{G}(\vec{r}_a, \vec{r}_b) = \mathbf{G}_0(\vec{r}_a, \vec{r}_b)\exp(-\mathrm{i}kM(\vec{r}_b - \vec{r}_a)\vec{e}_u) \tag{24}$$

where M is the Mach number $M = |\vec{U}|/c$, $\vec{e}_u = \vec{U}/U$ and $\mathbf{G}_0(\vec{r}_a, \vec{r}_b) = \frac{\exp(\mathrm{i}k|\vec{r}_a - \vec{r}_b|)}{4\pi|\vec{r}_a - \vec{r}_b|}$ is the Green function in a static homogeneous medium. Irreversibility is due to the fact that spatial reciprocity is no longer valid in this moving medium, i.e.

$$\mathbf{G}(\vec{r}_a, \vec{r}_b) \neq \mathbf{G}(\vec{r}_b, \vec{r}_a). \tag{25}$$

Acoustic irreversibility also appears in complex flows. However, in these flows the Green function is difficult to calculate. In order to interpret TR experiments, we present in this section some analogies between TR experiments conducted in acoustics, classical mechanics and electromagnetism.

3.1. Violation of time reversal invariance in classical mechanics and electromagnetism

In mechanics, TR invariance is valid only in a Galilean reference frame where the equation of motion of a particle (mass m) moving in a stationary potential $U(\vec{r})$ takes the form

$$-\vec{\nabla}U = m\frac{\mathrm{d}\vec{v}}{\mathrm{d}t}. \tag{26}$$

This equation is invariant under the transformation $t \to -t$, $\vec{v} \to -\vec{v}$ which implies that the path of the particle is reversible.

In non-Galilean frames, inertial effects such as the Coriolis force break the symmetry and complicate the issue. In a rotating frame of angular velocity $\vec{\Omega}$, the Coriolis force, given by

$$\vec{F}_c = 2m(\vec{v} \wedge \vec{\Omega}). \tag{27}$$

must be introduced in the equation of motion which is no longer invariant under the transformation $t \to -t, \vec{v} \to -\vec{v}$. Introducing a mirror of the time variable, which reverses the velocities of particles, gives rise to new particle paths which are no longer identical to the initial ones. The well known Foucault pendulum shows the Earth's rotation through the asymmetry between the direct and reverse paths. To achieve TR in a rotating frame also requires reversing the angular velocity of the reference frame: $\vec{\Omega} \to -\vec{\Omega}$.

Another example of violation of the TR symmetry appears when a charged particle (charge q) travels through a magnetic field $\vec{B}$. In this case, the magnetic Lorentz force applied to the charged particle,

$$\vec{F}_L = q(\vec{v} \wedge \vec{B}) \tag{28}$$

has the same effect as the Coriolis force on TR. To keep the path of the particle identical through a time mirror requires reversal of the magnetic field also: $\vec{B} \to -\vec{B}$.

These examples emphasize the strong analogy between the magnetic field and the angular velocity of the rotating frame.

3.2. Violation of time reversal invariance in acoustics

In analogy with mechanics, violation of the TR symmetry appears in acoustics when the medium of propagation contains a flow $\vec{U}$.

First, when the characteristic scale of the flow L is much larger than the acoustic wavelength λ, geometrical acoustics is valid. In this case, acoustic rays follow, at small Mach number, an equation analogous to the equation of motion of particles submitted to the Coriolis force in a rotating frame:

$$\frac{\mathrm{d}\vec{n}}{\mathrm{d}t} = -\vec{n} \wedge \vec{\Omega} \tag{29}$$

where $\vec{\Omega} = \overrightarrow{\mathrm{rot}}(\vec{U})$.

When geometrical acoustics is no longer valid, Lund [41] describes acoustic propagation through any flow with the equation

$$\Delta p - \frac{1}{c^2}\frac{\partial^2 p}{\partial t^2} = \mathrm{div}\left(\rho\vec{u} \wedge \vec{\Omega} + \vec{u}\frac{\partial \rho}{\partial t} - \rho\vec{\nabla}\left(\frac{1}{2}u^2\right)\right) \tag{30}$$

where $\vec{u}$ is the total velocity field (acoustic wave + flow) and ρ is the fluid density. In this formalism, $\vec{n}(\vec{r}, -t)$ or $p(\vec{r}, -t)$ are no longer solutions of equations (23) or (24). However, if TR is combined with the transformation $\vec{\Omega} \to -\vec{\Omega}$ or $\vec{U} \to -\vec{U}$, then acoustic propagation remains reversible.

Finally, even if the Green function is not computable in complex flows, a particular reciprocity relation still exists. In section 1.1, we showed that reversibility requires spatial reciprocity and invariance under time inversion. In an irrotationnal flow of velocity $\vec{U}$, the spatial reciprocity relation is changed to [42]

$$G_{\vec{U}}(\vec{r}, t|\vec{r}', t') = G_{-\vec{U}}(\vec{r}', -t'|\vec{r}, -t) \tag{31}$$

where $G_{\vec{U}}$ is the Green function in presence of the flow. Equation (31) confirms that, in a flow, reversibility occurs if time inversion is combined to the transformation $\vec{U} \to -\vec{U}$.

In a first series of experiments, Roux studied [43] violation of acoustic reversibility through a rotating cylinder immersed in a water tank. The cylinder is made of a viscoelastic material

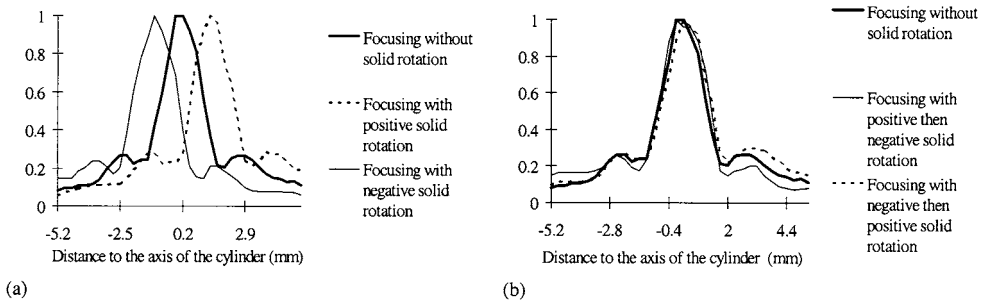

Figure 16. Deflection of the focal spot (*a*) after a constant solid rotation, (*b*) when the TR process is combined with the change of the sign of the solid rotation.

whose acoustical impedance is that of water. A single transducer and a TRM are placed on both sides of the rotating cylinder. When TR is performed on waves which have propagated through the medium in rotation, the focal spot is shifted from r_0 to a new position r_1 (figure 16(*a*)). For a rotation frequency of 50 Hz, the focal spot is shifted by 1 mm. The distance between r_0 and r_1 is proportional to the Mach number of the solid rotation. However, as expected, if the direction of rotation is changed after initial propagation, the time-reversed wave refocuses at r_0 (figure 16(*b*)). The main limitation encountered in this experiment is that it can only detect flows of large angular velocities.

3.3. The double TRM as a vorticity effect amplifier

In order to amplify the effect of vorticity on the acoustic wave, a system using a double TRM has been developed [44]. The double TRM is made up of two identical TRMs placed face to face, on both sides of the flow. The idea is to play a kind of TR ping-pong between the two TRMs. The first emission corresponds to a plane wave. Then, when one array emits an acoustic pulse, the other one receives, time reverses and re-emits the wave. In the absence of fluid motion, reversibility ensures that many consecutive back-and-forth propagations between the two arrays do not modify the emitted plane wavefront. However, in the presence of a vortex, the initially plane wave is slightly distorted at each crossing and this distortion increases linearly with the number of round trips. The analysis of this distortion allows one to solve the inverse problem, i.e. to determine the vorticity field of the flow. In fact, the double TRM appears as an artificial amplifier of vorticity effect: after N round trips through a vorticity field $\Omega(\vec{r})$, the wavefront shape is equivalent, to first order, to the shape obtained after a single crossing through a field with vorticity $2N\Omega(\vec{r})$.

3.3.1. Experiments on a large vortex. The experimental setup is shown in figure 17. The whole setup is used to create a large vortex (diameter $\sim$ 80 mm) near the bottom of the cylinder, stationary in the case of low angular velocity ($\Omega/2\pi \sim 1$ Hz). The two arrays of the double TRM are placed on a plane perpendicular to the axis of the solid rotation. Each array is made of 64 transducers and the total aperture of each array is about 25 mm.

Figure 18 shows the phase distortion at 3 MHz from -50 mm to 50 mm. A model based on geometrical acoustics describes quite simply the experimental results. In this approach, the wave velocity is locally modified by the flow velocity. At a given point in the flow, we add to the wave velocity, c, the component of the flow velocity projected on the acoustic ray. If $\vec{U}(\vec{r})$ is the flow velocity and $\vec{n}(\vec{r})$ the unit vector tangential to the acoustic ray at position $\vec{r}$,

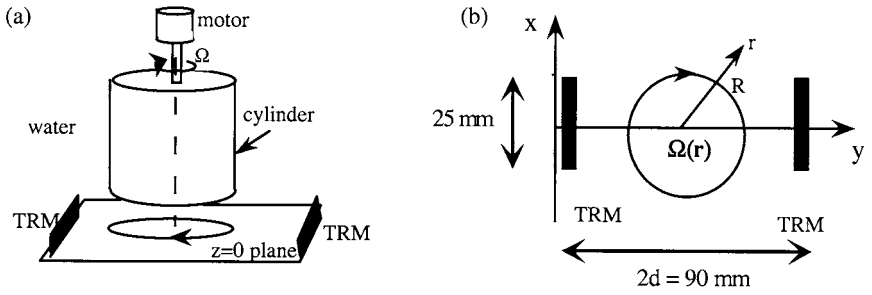

Figure 17. Experimental setup with a large vortex: (*a*) overall view, (*b*) double TRM in the $z = 0$ plane.

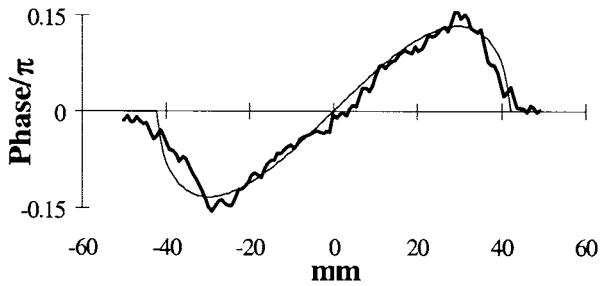

Figure 18. Phase distortion after eight round trips through a large vortex (thick curve), and predicted distortion using geometrical acoustics model (thin curve).

we can write the new local wave velocity $c'(\vec{r}) = c + \vec{U}(\vec{r}) \cdot \vec{n}(\vec{r})$. Moreover, in a first-order approximation, we can neglect the deflection of the wave by the vortex, leading to $\vec{n}(\vec{r}) = \vec{e}_y$. The phase shift measured in the x-direction after N round trips is

$$\frac{\Delta\varphi_N(x)}{2N} = -\frac{\omega}{c}\int_{-d}^{d} \frac{\frac{\vec{U}(\vec{r})\cdot\vec{n}}{c}}{1+\frac{\vec{U}(\vec{r})\cdot\vec{n}}{c}}\,\mathrm{d}y \tag{32}$$

where $2d$ is the distance between the two arrays and ω the angular frequency of the acoustic wave. Here, the large vortex is a flow in solid rotation such that $\vec{U}(\vec{r}) = \Omega r\vec{u}_\theta$ (where $\vec{u}_\theta$ is the angular unit vector). For small Mach number ($M \ll 1$), equation (26) can be simplified:

$$\frac{\Delta\varphi_N(x)}{2N} = -2\Omega\frac{\omega x}{c}\sqrt{R^2 - x^2}. \tag{33}$$

Equation (33) shows that the phase shift is proportional to the product $N\Omega$, which confirms that the TRM acts as a vorticity amplifier. In addition, the fit between the theoretical and the experimental phase shift (figure 16) allows us to calculate Ω and R ($\Omega/2\pi = 0.3$ Hz and $R = 42$ mm).

3.3.2. Experiments with vorticity filament: the acoustic Aharonov–Bohm effect. What happens now if the flow is induced by a vorticity filament? The experimental setup is as follows: a vorticity filament is generated in a cylinder ($R = 70$ mm) filled with water between a rotating disc placed at the top of the cylinder and a narrow tube at the bottom of the cylinder through which water is pumped out (figure 19(*a*)). The size of the vortex is typically of the same order as the size of the tube (2 mm diameter). As before, the double TRM is placed on

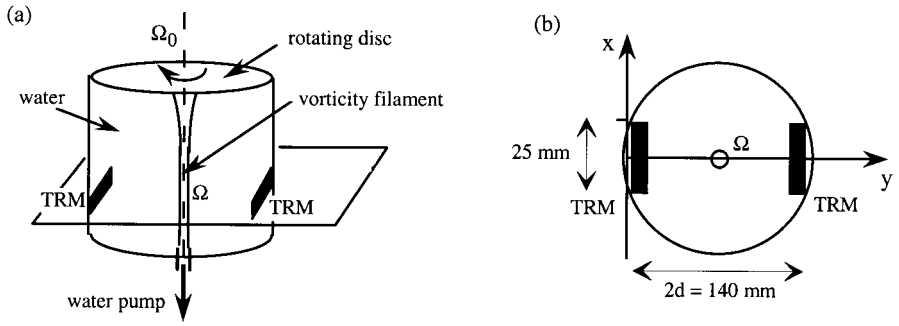

Figure 19. Experimental setup with a vorticity filament: (*a*) overall view, (*b*) double TRM in the $z = 0$ plane.

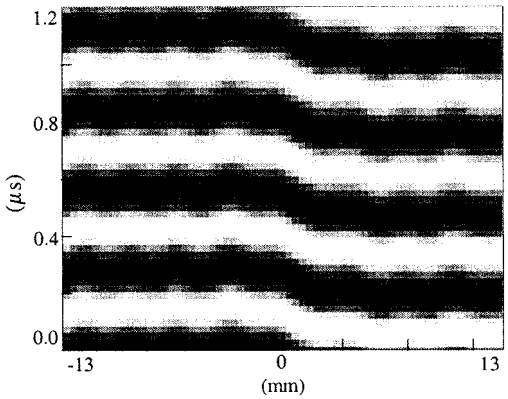

Figure 20. Distortion of an incident plane wave after a single crossing through a vorticity filament.

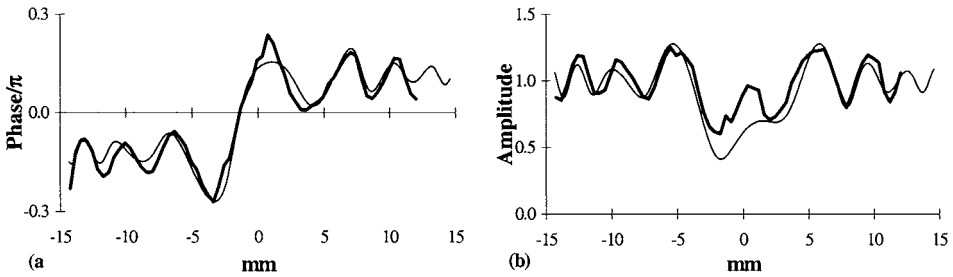

Figure 21. (*a*) Phase distortion and (*b*) amplitude distortion of a plane wave through an impenetrable vorticity filament: quantum approach (thick curve) and experimental measurements (thin curve).

both sides of the cylinder in a plane perpendicular to the axis of the vorticity field (figure 19(*b*)). Acoustically speaking, the vorticity filament is generally penetrable but, for strong suction, the filament becomes a little air tornado which is impenetrable. After a simple path through the vorticity field, the incident plane wavefront appears to be dislocated (figure 20). More precisely, figures 21(*a*) and (*b*) represent the phase and amplitude distortions at 3 MHz. Note that there is not only a phase dislocation but also a strong modulation of the phase and amplitude patterns. This can be interpreted as an interference between the dislocated wave and the wave scattered by the vortex core.

From a theoretical point of view, the dislocation effect can be predicted by a simple

geometrical acoustics model. Indeed, the vorticity filament creates a flow $\vec{U}(\vec{r}) = \frac{\Gamma}{2\pi r}\vec{u}_\theta$ outside the vortex core. Using equation (32), this induces

$$\frac{\Delta\varphi_N(x)}{2N} = 2\beta \tan^{-1}\left(\frac{d}{x}\right), \qquad \text{with} \quad \beta = -\frac{\omega\Gamma}{2\pi c^2}. \tag{34}$$

However, geometrical acoustics is no longer valid in the core of the vortex because the size of the filament is of the same order as the acoustic wavelength. In this case, the interaction may be studied using a full-wave approach based on the acoustical analogue of the Aharonov–Bohm effect [45]. Indeed, replacing vorticity by magnetic field, Berry *et al* [46] show that the Schrödinger's equation, which describes the quantum interaction between a beam of particles and a magnetic field confined in a filament, is the analogue, for small Mach number, of the sound propagation equation in a filamentary vorticity field. In the most general case, the quantum solution of the Schrödinger equation is quite complex [47]. However, in the case of an infinite magnetic string (which corresponds to a vorticity filament whose core is smaller than the acoustic wavelength), the far field solution is simple:

$$\Psi_\alpha(r,\theta) = \exp(-\mathrm{i}kr\cos(\theta) + \mathrm{i}\alpha\theta) - \sin(\pi\alpha)\frac{\exp(\mathrm{i}\frac{\theta}{2})}{\cos(\frac{\theta}{2})}\frac{\exp(\mathrm{i}kr + \mathrm{i}\frac{\pi}{4})}{(2\pi kr)^{1/2}}. \tag{35}$$

The acoustical analogue of the quantum parameter α is

$$\alpha = -\frac{\omega\Gamma}{2\pi\pi^2} = \beta \tag{36}$$

where Γ is the circulation of the flow. Finally, the analogies between quantum mechanics and acoustics have been summed up by Umeki and Lund [48] in the following table.

Quantum physics	Acoustics
magnetic field $B = \mathrm{curl}(A)$	field of vorticity $\Omega = \mathrm{curl}(U)$
vector potential A	velocity field of the flow U
magnetic flux ϕ	circulation Γ
wavefunction ψ	wavefunction ψ

The first term of the wavefunction Ψ_α describes the dislocation of the incident plane wave whereas the second term represents the wave scattered by the vortex core. For penetrable or impenetrable vortices of different core size, the fit between the quantum solution and the experimental measurements allows characterization of the vorticity field. For example, the data from figure 21 allows one to calculate the parameter $\alpha = 0.095$ and the radius of the vortex core $r_0 = 1.3$ mm.

4. The TRM in pulse echo mode

The most promising area for the application of TRMs is perhaps pulse echo detection. In this domain, one is interested in detection, imaging and sometimes destruction of passive reflecting targets. The low velocities of ultrasonic waves allows separation of reflecting targets at different depths. A piezoelectric transducer first sends a short impulse and then detects the various echoes from the targets. In nondestructive evaluation (NDE), cracks and defects can be found within materials of various shapes. In medical imaging, one looks for organ walls, calcification, tumours, kidney or gallbladder stones. In underwater acoustics, one looks for mines, submarines, or objects buried under sediments. In all of these cases, the acoustic detection quality depends on the availability of the sharpest possible ultrasonic beams to scan

the medium of interest. The presence of an aberrating medium between the targets and the transducers can drastically change the beam profiles. In medical imaging, a fat layer of varying thickness, bone tissue, or muscular tissue may greatly degrade focusing. In NDE, the samples to be evaluated are usually immersed in a pool and the interface shape between the samples and the coupling liquid currently limits the detectability of small defects. In underwater acoustics, refraction due to oceanic inhomogeneities ranging in scale from centimetres to tens of kilometres are important sources of distortions.

For all these applications, a TRM array can be controlled according to a three-step sequence [49]. One part of the array generates a brief pulse to illuminate the region of interest through the aberrating medium. If the region contains a point reflector, the reflected wavefront is selected by means of a temporal window and then the acquired information is time-reversed and re-emitted. The re-emitted wavefront refocuses on the target through the medium. It compensates also for unknown deformation of the mirror array. As has been shown, the TR processing is a realization of a spatiotemporally matched filter to the propagation transfer function between the array and the target. Although this self-focusing technique is highly effective, it requires the presence of a reflecting target in the medium.

4.1. Selective focusing through an inhomogeneous medium with the iterative time reversal process

4.1.1. The principle. In media containing several targets, the problem is more complicated and iterations of the TR operation may be used to select one target. Indeed, if the medium contains two targets of different reflectivities, the TR of the echoes reflected from these targets generates two wavefronts focused on each target. The mirror produces the real acoustic images of the two reflectors on themselves. The highest-amplitude wavefront illuminates the most reflective target, while the weakest wavefront illuminates the second target. In this case, the TR process can be iterated. After the first time-reversed illumination, the weakest target is illuminated more weakly and reflects a fainter wavefront than the one coming from the strongest target. After some iterations, the process converges and produces a wavefront focused on the most reflective target. It converges if the target separation is sufficient to avoid the illumination of one target by the real acoustic image of the other one [49].

Although this simple presentation of the iterative mode is very attractive, one can argue that a contradiction exists between the concept of iteration and the physical principle of TR invariance. Indeed, the complete TR of an acoustic 'scene' results in the time-reversed scene. Therefore, the iteration of the TR operation gives stationary results, a contradiction with wavefield modification after each iteration. In fact, the contradiction is only apparent. A complete TR operation requires a closed TRC surrounding the acoustic scene and a recording time T long enough to take into account all the multiple scattered waves. In our technique, we utilize only a finite spatial aperture and short temporal window. Therefore, some information is lost. This information loss gives the iterative mode its target selection capabilities.

4.1.2. Experiments. Experiments have been performed with a linear array of central frequency 3.5 MHz as described in section 2.2. They demonstrate the ability of TRM in iterative mode to select the most reflective target in a multiple target medium. The medium was made of two different wires situated at a depth $z = 90$ mm from the array. The two wires were parallel to the long axis of each array element and they were located on either side of the array axis. A 0.2 mm diameter copper wire was located at 5 mm from the array axis and a 0.4 mm copper wire was located at 5 mm on the opposite side of the axis. An aberrating layer was placed between the array and the two wires (figure 22).

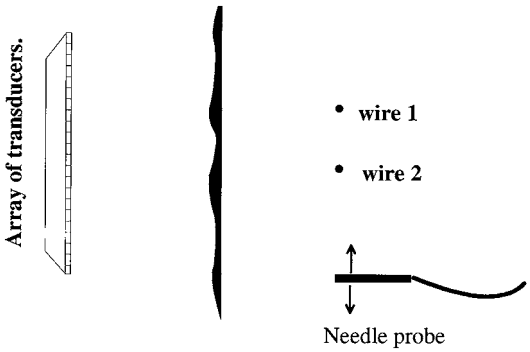

Figure 22. Experimental setup.

In the first step, one transducer of the array illuminates an angular sector containing the two wires. The illuminated beam is transmitted by a single transducer element located at the array centre. The directivity pattern of a single element is wide. After the first illumination, the echoes from the two targets are recorded. Figure 23(*a*) shows the recorded data corresponding to two individual wavefronts pointing at the two wires. The recorded signals are then time reversed and retransmitted. The time-reversed waves propagate and the new directivity pattern is measured by scanning the plane $z = 90$ mm with the hydrophone. The solid curve of figure 24 represents the directivity pattern which shows two maxima corresponding to the two target locations. The pressure field reaches a higher value at the location of the wire whose scattering cross section is larger. The process is iterated: the new echoes from the wires were recorded, time reversed and retransmitted, etc. As the process is iterated, the wire which reflects less energy receives a weaker time-reversed wave. This is shown in figure 24 which corresponds to the directivity pattern of the first to the fourth iteration. The small wire is no longer illuminated after the last emission. Figure 23(*b*) represents the reflected wavefronts recorded by the array after the fourth iteration (note that the wavefront has a longer duration because of the multiple iterations, which implies a repeated effect of the acousto-electric transducer response).

These experiments demonstrate the ability of TRM iterative mode to select the most reflective target in a multiple target medium. This may be interpreted as a learning process that selects among several wavefronts the one coming from the most important reflector.

4.2. Theory of the iterative time reversal process

Prada *et al* [50] has studied theoretically the convergence of the iterative TR process and has derived conditions for selecting the most reflective target in a multiple target medium. However, in some cases one may want to focus on the other reflectors. The theoretical analysis of the iterative TR process led to a solution for this problem which is developed in section 4.4.

This analysis is briefly presented in the following section. In order to understand the convergence of the iterative TR process, a matrix theory was constructed. First a transmit–receive operation is described in a general manner, defining the transfer matrix of the system. Then, the TR operator is introduced.

4.2.1. The transfer matrix. We consider an array of transducers insonifying a given scattering medium. As for all ultrasonic imaging devices, the system is assumed to be linear. Furthermore, it is assumed to be time invariant during the iterative TR process. Such a system can be described by its impulse response functions. If N is the number of transducers in the array, there are $N \times N$ inter-element impulse response functions $h_{lm}(t)$ defined as the signal delivered

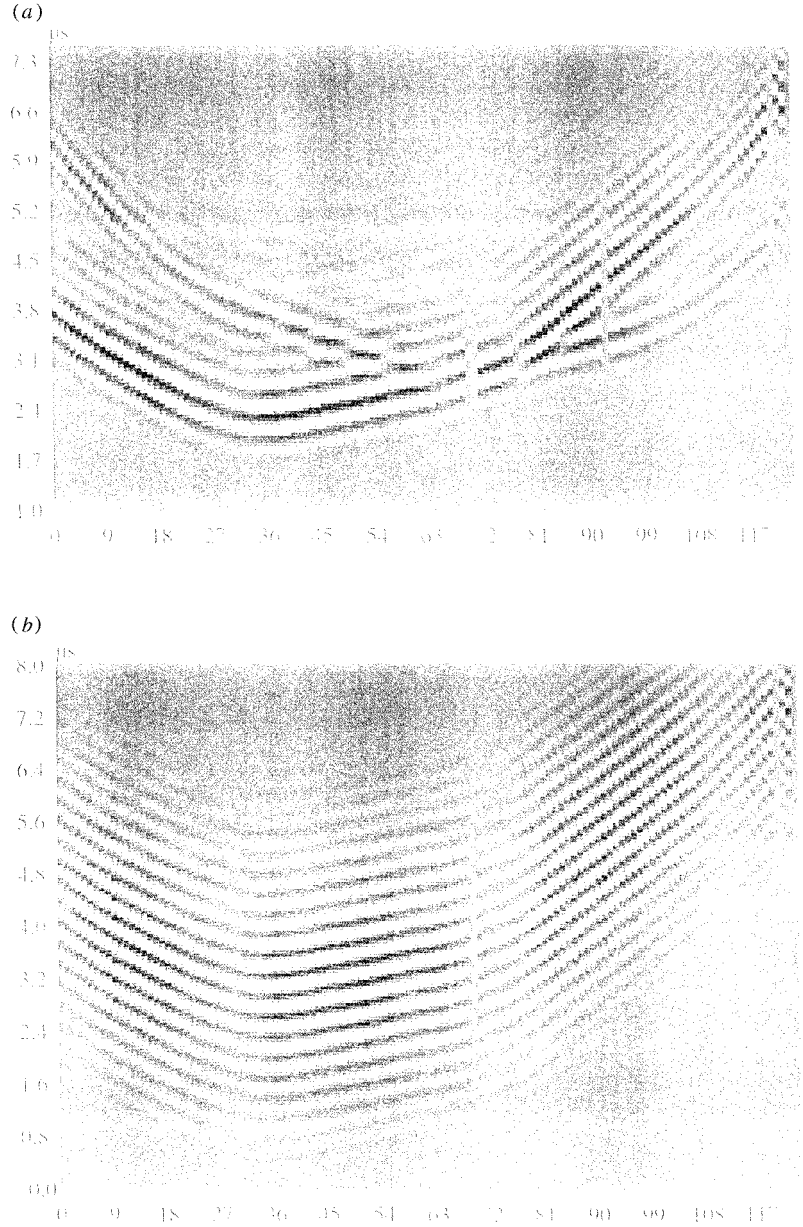

Figure 23. (*a*) Echographic signals observed from the two wires after the first illumination. (*b*) Echographic signals observed after four iterations of the TR process.

by transducer number l when a temporal delta function is $\delta(t)$ applied on the transducer number m. These N^2 signals provide a complete description of the system. Indeed, if $e_m(t) 1 \leqslant m \leqslant N$ are the transmitted signals then the received signals $r_l(t)$ $1 \leqslant l \leqslant N$ are given by the equation

$$r_l(t) = \sum_{m=1}^{N} h_{lm}(t) \underset{t}{\otimes} e_m(t). \tag{37}$$

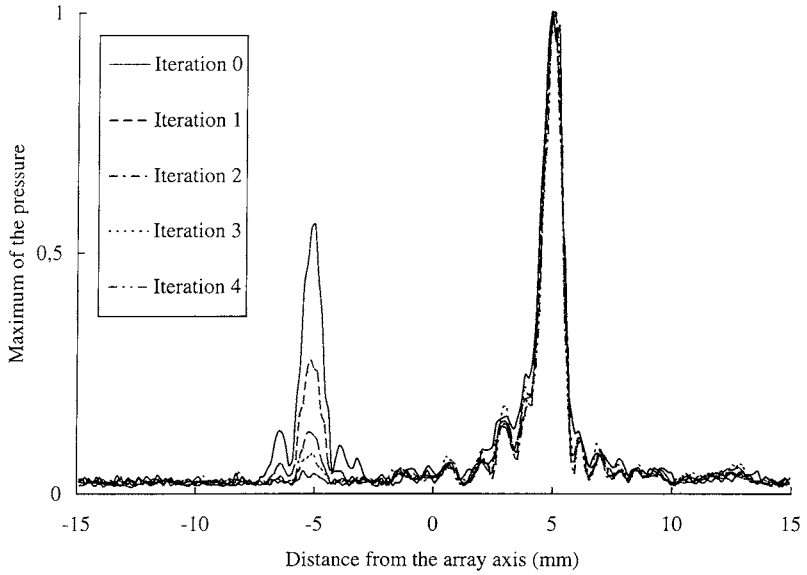

Figure 24. Directivity patterns measured in the wire plane after each iteration.

In the frequency domain, this equation takes on a simple matrix form

$$R(\omega) = \boldsymbol{H}(\omega)E(\omega) \tag{38}$$

where $E(\omega)$ and $R(\omega)$ are the transmitted and the received vector signals of N complex components, and $\boldsymbol{H}(\omega)$ is the $N \times N$ complex *transfer matrix* of the system.

4.2.2. The iterative time reversal process. Using this matrix formulation, the TR process can now be described. The matrix relation between transmitted and received signals leads to an expression of the transmitted signals at each iteration of the process. A TR operation $t \rightarrow -t$ is equivalent to a phase conjugation in the frequency domain so that if $E_0(\omega)$ is the first transmitted signal of an iterative TR process then the second transmitted signal is the phase conjugate of the received signals

$$E_1(\omega) = \boldsymbol{H}^*(\omega)E_0^*(\omega). \tag{39}$$

After two TR operations the transmitted signal depends linearly on the first transmitted one as follows:

$$E_2(\omega) = \boldsymbol{H}^*(\omega)\boldsymbol{H}(\omega)E_0(\omega), \tag{40}$$

and after $2n$ TR operations the transmitted signal is

$$E_{2n}(\omega) = [\boldsymbol{H}^*(\omega)\boldsymbol{H}(\omega)]^n E_0(\omega). \tag{41}$$

$\boldsymbol{H}^*(\omega)\boldsymbol{H}(\omega)$ is called the TR operator.

As a consequence of the reciprocity theorem, the inter-element impulse response from element number m to element number l is equal to the inter-element impulse response from element number l to element number m so that the transfer matrix is symmetrical.

Due to the symmetry of $\boldsymbol{H}(\omega)$, the TR operator is Hermitian with positive eigenvalues. Let $V_1(\omega)$ be the projection of $E_0(\omega)$ on the eigenspace of the highest eigenvalue $\lambda_1(\omega)$ (in

general $V_1(\omega)$ is nonzero). For large values of n the transmitted signal after $2n$ iterations of the TR process is

$$E_{2n}(\omega) \approx \lambda_1(\omega)^n V_1(\omega). \tag{42}$$

In practice, at each iteration of the TR process, the coefficient $\lambda_1(\omega)$ is compensated by some amplification, so that the signal remains finite. So we see that the iterative TR process is convergent and the limit is proportional to $V_1(\omega)$. The convergence is geometrical depending on the ratio of the highest and the second highest eigenvalue $\lambda_1(\omega)/\lambda_2(\omega)$.

We need now to give a physical interpretation of these mathematical results and this can be done in the case of pointlike well resolved scatterers.

4.2.3. The case of pointlike scatterers.

The transfer matrix. In the case of pointlike scatterers the transfer matrix can be derived easily. We assume that the medium contains d pointlike scatterers with complex frequency-dependent reflectivity coefficients $C_1(\omega), C_2(\omega), \ldots, C_d(\omega)$. Then the transfer matrix can be written as the product of three matrices: a propagation matrix that describes the transmission and the propagation from the transducers to the scatterers, a scattering matrix which is diagonal in the case of a single-scattering process and the backpropagation matrix.

Let $h_{il}^d(t)$ be the diffraction impulse response function of the transducer number l to the scatterer number i with Fourier transform $\boldsymbol{H}_{il}^d(\omega)$. Let $a_e(t)$ and $a_r(t)$ be the transducer acoustoelectrical responses in transmit and in receive mode, with Fourier transforms $A_e(\omega)$ and $A_r(\omega)$. If the input signal at each element l is $e_l(t)$, then the pressure at the scatterer i is

$$p_i(t) = \sum_{l=1}^{N} h_{il}^d(t) \underset{t}{\otimes} a_e(t) \underset{t}{\otimes} e_l(t). \tag{43}$$

This equation is written in the frequency domain using a matrix notation:

$$P = A_e \boldsymbol{H}^d E \tag{44}$$

where E is the input vector signal, P is the vector representing the pressure received by the d scatterers and $\boldsymbol{H}^d$ is a matrix of dimensions $N \times d$ called the diffraction matrix.

In the case of single scattering, the pressure reflected by scatterer number i is $C_i P_i$. Therefore, the vector of reflected pressures is $C P$ where C is a diagonal matrix of coefficients $C_{ij} = \delta_{ij} C_i$ $(i, j \in 1, \ldots, d)$.

According to the reciprocity principle, the propagation from the scatterer number i to the transducer number l is also $h_{il}^d(t)$, so that the backpropagation matrix is the transpose of the propagation matrix $\boldsymbol{H}^d$. Consequently, the output signal is $R = A_e A_r^t \boldsymbol{H}^d \boldsymbol{C} \boldsymbol{H}^d E$.

Therefore, the expression of the transfer matrix is

$$\boldsymbol{H} = A_e A_r^t \boldsymbol{H}^d \boldsymbol{C} \boldsymbol{H}^d. \tag{45}$$

In the following, we shall omit the scalar term $A_e A_r^t$.

Diagonalization of the time reversal operator for ideally resolved scatterers. The scatterers are well resolved if it is possible to focus on any one of them, sending little energy to the others. More precisely, we say that they are 'ideally resolved' if the TR focusing on one of them does not produce energy on the others. From the mathematical point of view, this means that the rows of the propagation matrix $\boldsymbol{H}^d$ are orthogonal.

In that case, it is straightforward to determine the eigenvectors of $\boldsymbol{H}^*(\omega)\boldsymbol{H}(\omega)$ (the detailed proof can be found in [50, 51]). They are the vectors

$$H_i^{d*}, \qquad 1 < i < d$$

complex conjugate of the columns of the matrix $\boldsymbol{H}^d$ associated to the eigenvalues

$$\lambda_i = |C_i|^2 \left(\sum_{l=1}^{L} |H_{il}^d|^2 \right)^2, \qquad 1 < i < d. \tag{46}$$

H_i^{d*} is exactly the signal that would be transmitted to the array in a TR process if the scatterer number i was alone. The eigenvalue λ_i is the square of the apparent reflectivity $\alpha_i = C_i \sum_{l=1}^{L} |H_{il}^d|^2$ which depends on the position of the scatterer with respect to the transducer array. Thus, the eigenvector of highest eigenvalue corresponds to the scatterer of highest apparent reflectivity.

This result confirms theoretically what we have shown in experiment (section 4.1.2): for ideally resolved scatterers, the iterative TR process converges toward the focusing on the scatterer of highest apparent reflectivity.

4.3. Inverse scattering analysis and elastic target resonance

Beside their usefulness for the detection of reflecting objects, TRMs afford a new means to carry out an inverse scattering analysis on a spatially extended elastic target, in other words to characterize a scatterer from the knowledge of its scattered field. The same analysis leads to a technique to put an elastic target in resonance.

The interaction of a short ultrasonic beam with an extended solid target produces a backscattered field with several components. A first reflected wave called the specular echo, which would be obtained if the target was perfectly rigid, is determined by the target geometry. That is followed by a series of waves—the so-called elastic echo—due to the propagation of surface and volume waves around and inside the scatterer. These waves are generated at particular points on the target, propagate at the surface or in the solid and then radiate into the fluid from different mode-conversion points on the scatterer that act as secondary sources. Thomas [52] has studied the case of a thin air-filled hollow cylinder off which the elastic part of the acoustic scattering is mainly due to circumferential waves (dispersive Lamb waves): the first symmetrical and antisymmetrical Lamb waves S_0 and A_0. Because these two waves have different velocities, they can be separated experimentally by time windows. They are generated at different points on the target in accordance with Snell's law. As the two waves are weakly dispersive and have different velocities, they are easily separated experimentally by time windowing.

Each one of these waves is generated at a given angle of incidence θ with respect to the normal to the surface. This angle satisfies the relation

$$\sin(\theta) = \frac{c_0}{c_\phi} \tag{47}$$

where c_0 is the sound speed in water and c_ϕ is the phase velocity of the Lamb wave. While propagating around the cylinder, they radiate into the fluid at opposite angle with respect to the normal to the surface. For an incident plane wave, two Lamb waves are generated at points A and B which are symmetric with respect to the incident direction (figure 25). Those two waves radiate backward from the same points A and B. The distance d_{AB} between those points is given by

$$d_{AB} = D\frac{c_0}{c_\phi}. \tag{48}$$

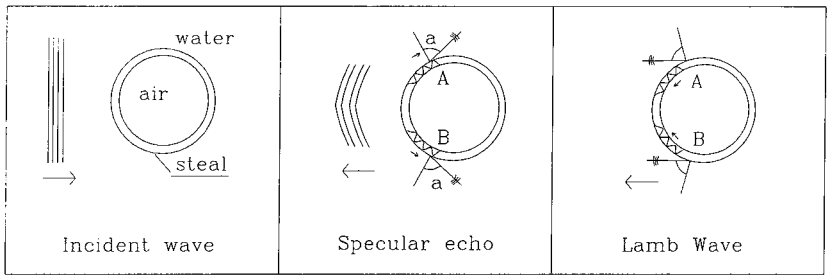

Figure 25. Generation and radiation of a Lamb wave on a thin hollow cylinder.

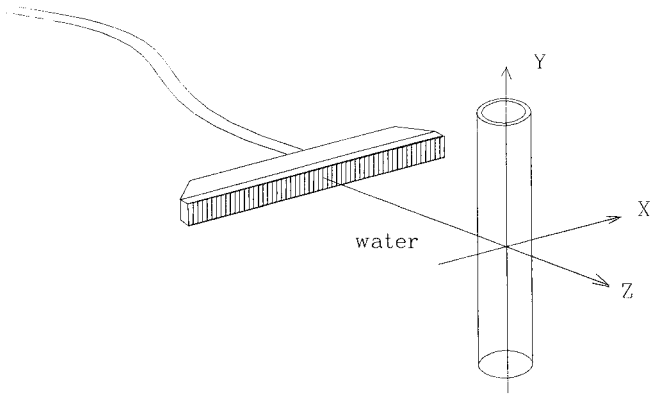

Figure 26. Experimental setup.

Experiments have been conducted with a linear array of 128 transducers identical to the one described in section 2.2 on a steel cylinder of diameter 20 mm and thickness approximately 0.6 mm. The cylinder axis is perpendicular to the array of transducers and is located at a depth of 80 mm (figure 26). A short pulse is launched by the centre element of the array. The signal scattered by the cylinder is recorded on the whole array. The signal is composed first of the strong specular echo and then of the elastic echo (figure 27). On the elastic part, two pairs of wavefronts with interference fringes can be seen. Those wavefronts correspond to the different circumferential waves that have turned once around the shell. The first one is identified as the S_0 Lamb wave, the second one as the A_0 Lamb wave. The symmetry of the fringes with respect to the array axis reveals the two symmetric pointlike sources. Each pair of sources can be associated with one surface wave. To confirm this observation, a time window selects the first echo in the elastic part of the signal. This echo is time reversed and the time-reversed field is scanned with a needle hydrophone along a line perpendicular to the cylinder axis. At each location of the hydrophone, the time dependence of the pressure is recorded. The directivity pattern which represents the maximum of the pressure field (figure 28) shows two symmetrical lobes. The distance between them corresponds to a phase velocity of 5.1 mm μs^{-1} which confirms that corresponding to the wave S_0. The same process is applied to the second part of the elastic echo. In this case, the distance between the lobes is 11 mm, it corresponds to a phase velocity equal to 2.3 mm μs^{-1} which is the velocity of the A_0 Lamb wave.

The TR process can also be applied to generate selectively one of the circumferential waves. In this case the selected time-reversed field is transmitted without removing the cylinder. The time-reversed wave is spatially adapted to the chosen circumferential wave, its energy is

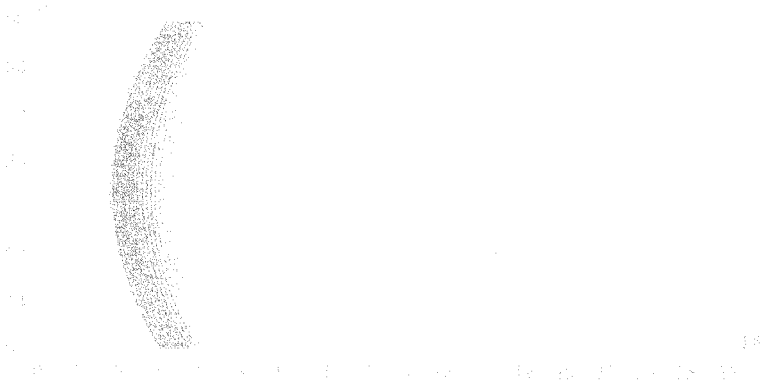

Figure 27. Echo of the shell received by the 128 transducers after transmission of a short pulse by the centre element of the array. The first wavefront is the specular echo, the second is the contribution of the S_0 Lamb wave and the third the contribution of the A_0 Lamb wave.

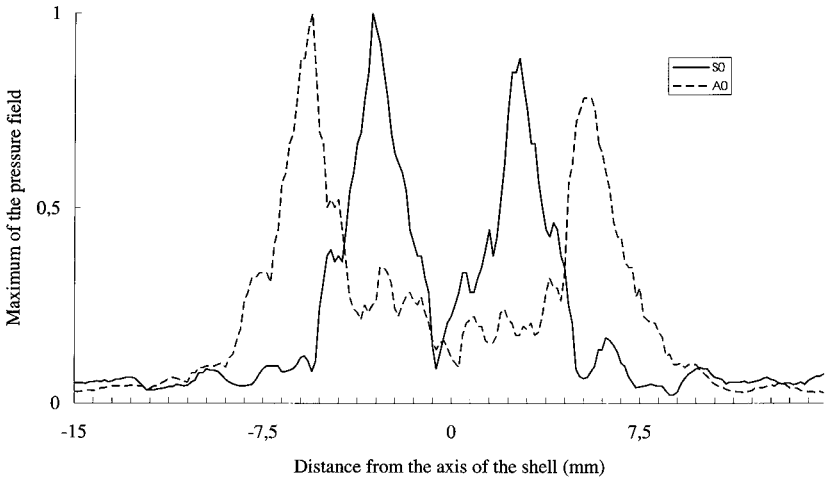

Figure 28. Directivity pattern measured in the plane of the shell after TR of the echo corresponding to the A_0, S_0 Lamb waves.

focused on its two generation points. The enhancement of the corresponding wave can be seen on the new echo coming from the cylinder. The elastic part of the echo is dominated by the selected wave as shown in figure 29 for the A_0 wave and in figure 30 for the S_0 wave. The A_0 wave is attenuated very quickly (it has a high radiation coefficient) so that only one turn around the shell can be seen, but the S_0 wave propagates several times around the shell and the contribution of three turns can be seen on the echo.

4.4. The DORT method

Generally, the scattering of ultrasound is complicated: the incident wave is converted into different types of waves which contribute to the scattered field. In order to understand the scattering process and to relate it to the characteristics of the medium, it is necessary to separate the different contributions from the signal. In many cases, the separation can be done using highly resolved broadband pulses. However it may occur that the signals overlap in time and cannot be separated by a time window.

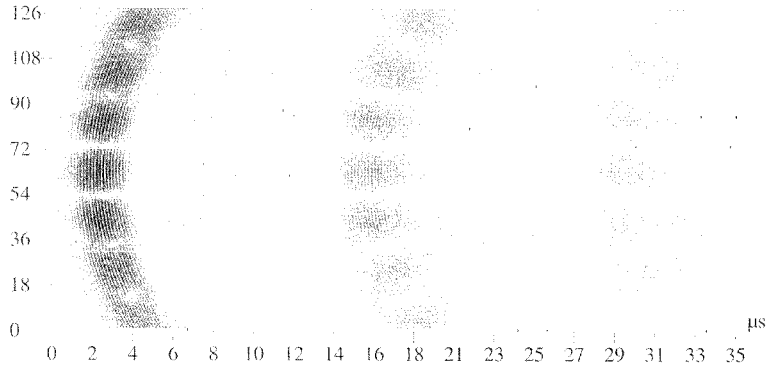

Figure 29. Echo of the shell after TR of the S_0 wavefront.

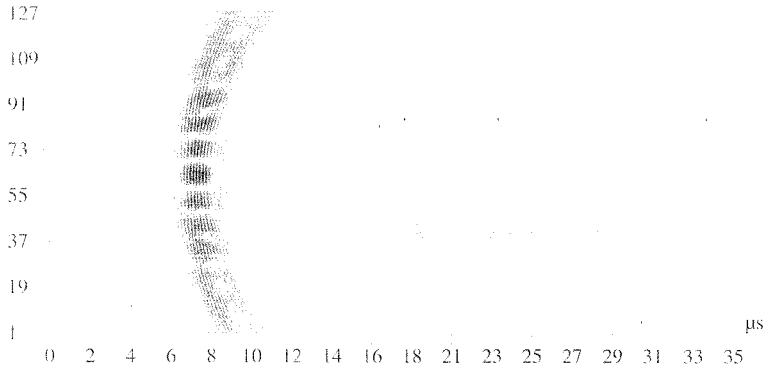

Figure 30. Echo of the shell after TR of the A_0 wavefront.

In some cases, the construction of the invariants of the TR process allows one to achieve the separation of the different waves which contribute to the scattered field. The construction of these invariants is the major part of the DORT method (DORT is the French acronym for 'décomposition de l'opérateur de retournement temporel').

One important application of this method is selective focusing in a multiple-target medium. Indeed, it was shown that the iterative TR process allows selective focusing on the most reflective of a set of scatterers. But in many cases it is of interest to focus on the other scatterers. Lithotripsy, when several kidney stones exist, is an example. The theoretical analysis of the iterative TR process has led to a solution to this problem (section 4.1) which has motivated the implementation of the DORT method [51, 53].

4.4.1. Principle. The DORT method is performed in three steps. *The first step* is the measurement of the inter-element impulse responses of the system. Since the receiving system operates in parallel, this measurement requires N transmit–receive operations for an array of N transducers. The first transducer of the array is excited with a signal $e(t)$ and the signals received on the N channels are stored. This operation is repeated for all the transducers of the array with the same transmitted signal $e(t)$. The components of the transfer matrix $H(\omega)$ are obtained by a Fourier transform of each signal. This measurement could also be done with any multiplexed system by N^2 transmit–receive operations. *The second* step is the diagonalization of the TR operator $H^*(\omega)H(\omega)$ at a chosen frequency. The eigenvalue

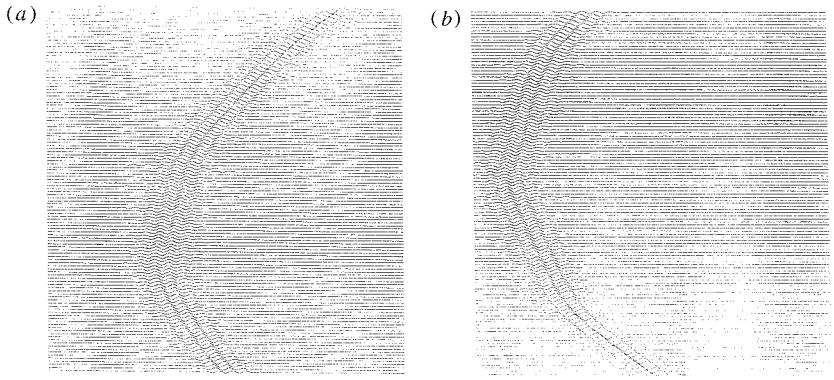

Figure 31. Acoustic signals obtained from the two eigenvectors.

distribution thus obtained contains valuable information, including the number of secondary sources in the scattering medium. *The third step* is to backpropagate the main eigenvectors. In many cases, when the propagation medium is known, it can be done numerically. This provides interesting information on the scattering process (section 4.4.3). As presented in the next section, the backpropagation can also be done experimentally to achieve selective focusing through inhomogeneous media.

4.4.2. Selective focusing through an inhomogeneous medium with the DORT method. As shown in section 4.2.3, if the scattering medium contains a number d of Rayleigh scatterers ideally resolved, the invariants of the TR operator are the vector signals that would be transmitted after one TR process if only the target number i was present. Consequently, for well resolved pointlike scatterers the number of nonzero eigenvalues is equal to the number of scatterers. Furthermore, if the scatterers have different 'apparent reflectivities', each eigenvector is associated to one scatterer and its phase and amplitude are the one to be applied on each transducer in the array in order to focus on that scatterer.

The experimental setup was similar to the one presented before to illustrate the efficiency of the iterative TR process (section 4.1.2). The inter-element impulse responses were measured and the TR operator was computed at the frequency of 3 MHz. Its diagonalization revealed two significant eigenvalues. Two sets of acoustic signals were built from the corresponding eigenvectors (figure 31) and they were transmitted through the medium. The resultant pressure field was measured with a hydrophone in the plane of the wires. Each eigenvector focuses on one of the wires (figure 32). The quality of the focusing is similar to that obtained in plain water [53].

4.4.3. Application of the DORT method to an inverse problem (cylindrical target). The preceding experiment shows the ability of the DORT method to focus selectively on different scatterers through an inhomogeneous medium. But more generally this method isolates and classifies the scattering centres or secondary sources in the medium and can be used to analyse the scattering from extended objects. Consequently, this method is applicable to the problem of a thin hollow cylinder, previously treated with the TRM (section 4.3) [54].

Circumferential waves and invariants of the time reversal process. As we mentioned in section 4.3, the two circumferential waves generated in A and B are linked by reciprocity.

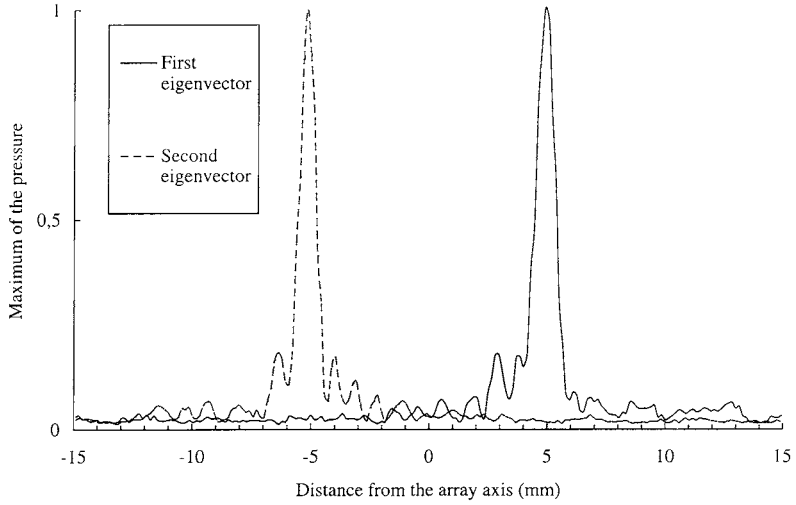

Figure 32. Directivity patterns measured in the wire plane from the transmission of each individual eigenvector.

The first one can be obtained by TR of the second one. Both waves are invariant under two successive TR processes, consequently they should be associated to eigenvectors of the TR operator. In fact, due to the symmetry of the problem, they are both associated with the same two eigenvectors: one corresponding to the generation in phase of the two waves and the other to the generation in opposite phase.

The cylinder and the transducer array used for this experiment are similar to the one used in the previous section except that only 96 transducers were used. On the elastic part of the signals displayed in figure 27, the two pairs of wavefronts correspond to the S_0 and the A_0 Lamb mode. In fact, at this frequency, three Lamb waves might be observed: A_0, A_1 and S_0. However, the A_1 wave is so dispersive in this frequency range that its contribution to the scattered field interferes with the contributions of A_0 and S_0 and can hardly be separated.

The 96×96 inter-element impulse responses have been measured and only the elastic part of the signal was used to compute the TR operator. At 3.05 MHz, the diagonalization of the TR operator shows six dominant eigenvalues. The moduli of the components of each eigenvector (1 to 6) are represented versus array elements (figure 33). The interference fringes are easily observed. They are the equivalent at a certain frequency of the interference pattern observed on the echoes. This shows that an eigenvector corresponds to the interference of two coherent point sources.

The numerical backpropagation of each eigenvector confirms this analysis and allows one to determine the distance between the sources (figure 34). Each pair of sources corresponds to one particular wave. At this frequency, the first and second eigenvectors are associated to the wave S_0, the third and fourth to the wave A_1 and the fifth and sixth to the wave A_0.

The same calculation is done at several frequencies from 2.2 to 4 MHz so that the dispersion curves for the three waves can be plotted (figure 35). These curves are very close to the theoretical curves obtained for a steel plate of thickness of 0.6 mm. In particular, the determination of the cut-off frequency of the A_1 wave allows one to infer the thickness of the shell.

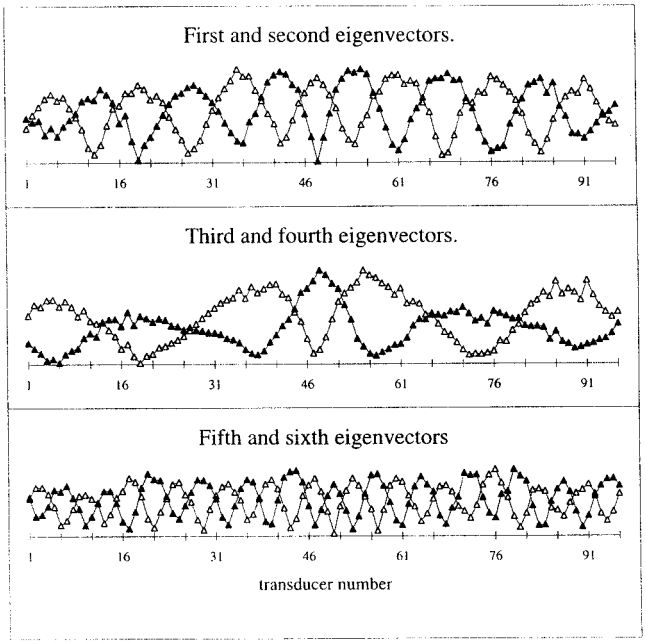

Figure 33. Modulus of the components of the six eigenvectors.

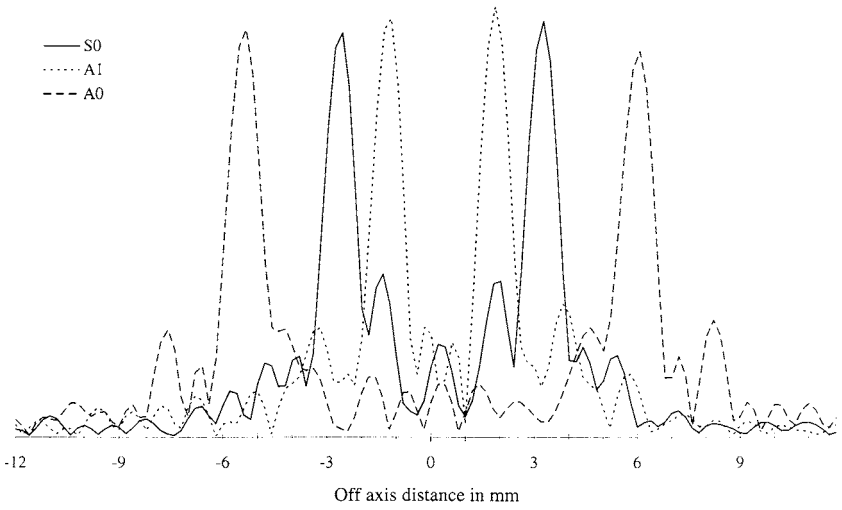

Figure 34. Directivity patterns obtained by numerical propagation of eigenvectors 1, 3 and 5.

Spectrum of the time reversal operator and resonance frequencies. The eigenvalue associated with one particular wave depends on the frequency, and is proportional to the contribution of the wave to the scattered field. In addition to the responses of the transducers, the generation and re-radiation coefficients of the wave are responsible for these variations. Moreover, if the duration and the level of the recorded signals allow one to detect several turns of the wave around the shell, a fast modulation of the corresponding eigenvalue is induced, the maxima corresponding to the resonance frequencies of the shell. In the experiment, the A_0 wave is

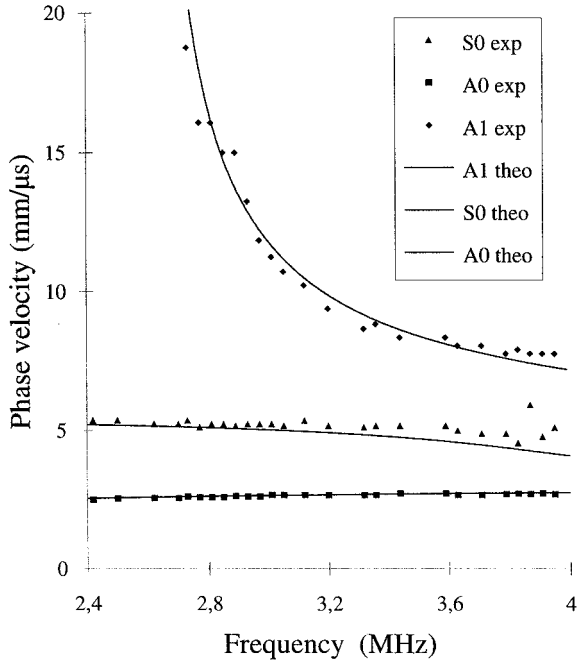

Figure 35. Dispersion curves: theory and experiment.

attenuated so fast that only one turn can be observed. But several turns of A_1 and S_0 contribute to the scattered field. The first six eigenvalues (denoted by $\lambda_1(\omega) \ldots \lambda_6(\omega)$) of the TR operator are represented versus frequency (figure 36). The two curves $\lambda_1(\omega)$ and $\lambda_2(\omega)$ correspond to the wave S_0. Their maxima occur at the resonance frequencies of the shell corresponding to this wave. The width of the peaks is mainly due to the length and the dynamics of the recorded signals which allow one to see only three turns of S_0 wave around the shell. Similar observations can be made for the A_1 wave. This wave is associated to the eigenvalues $\lambda_3(\omega)$ and $\lambda_4(\omega)$ around its resonance frequencies and to $\lambda_5(\omega)$ and $\lambda_6(\omega)$ near its anti-resonance frequencies. The DORT method provides the resonances frequencies due to the waves S_0 and A_1, with the great advantage that close resonance frequencies can be distinguished.

4.4.4. Application of the DORT method in a waveguide. Recently, the DORT method has been extended to waveguide propagation [55]. Taking advantage of the multiple reflections at the waveguide interfaces, the method was used to separate the signal coming from different scatterers and then to focus a wavefield at any one of them. For the waveguide described in section 2.3, the resolution obtained was nine times better than the free-space diffraction prediction. Moreover, it was shown that a combination of the eigenvectors found at each frequency provided the time domain impulse responses of each scatterer to the array. These experimental results suggest several lines of research. The DORT method could be applied to target detection and imaging in nondestructive testing in solid waveguides as well as in waveguide propagation in the ocean. The method was also applied to the detection of a scatterer near the water/air interface, the depth at which the scatterer is no longer detectable was shown to be less than one-fifth λ at a range of 400λ. The efficiency of the method in a nonstationary waveguide was also studied, and it has been shown that averaging of the transfer matrix allowed one to reduce the noise singular values and to keep a resolution almost three

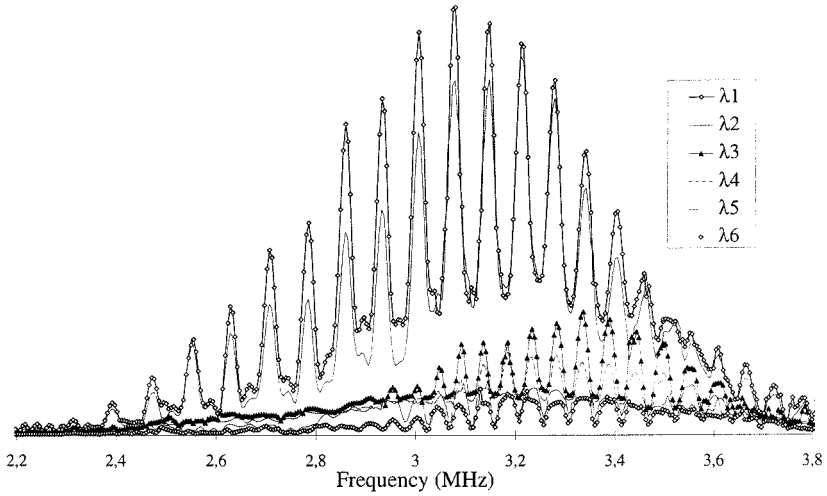

Figure 36. Eigenvalues of the TR operator versus frequency.

times thinner than in free space. The results presented in a nonstationary guide are promising and motivate further studies of underwater applications such as mine countermeasures.

5. Medical applications of TRMs

The adaptive focusing property of TRMs has great potential for improving the efficacy of medical application of ultrasound. Indeed, most ultrasonic therapeutic or imaging systems use transducer arrays and assume a constant acoustic velocity in human tissues of typically 1520 m s^{-1}. Electronic steering and focusing of the transducer arrays are implemented by calculating for each point of the zone of interest the corresponding time delay law. Over recent years, image improvements in medical scanners have been achieved mainly by increasing the focusing aperture dimension. However, as the aperture increases, the basic assumptions of a nearly homogeneous medium fail and the effects of inhomogeneities gain importance. Different authors [56–60] have investigated the degradation of ultrasonic beams due to abdominal wall, liver and breast. They have shown that the image quality improvement due to increased apertures is limited by these inhomogeneities. They also provide data about wavefront distortions including phase and amplitude distortion caused by tissue. In the human body, sound velocity varies from 1440 m s^{-1} in fat to above 1580 m s^{-1} in muscles and 1675 m s^{-1} in connective tissues. As an ultrasonic wavefront propagates through inhomogeneous tissues it is distorted, resulting in a spreading of the beam and an energy shift from the main lobe towards the side-lobes. These effects decrease image contrast or heating patterns and degrade spatial resolution, thus obscuring important diagnostic information or reducing therapeutic performance.

In a first attempt to solve these problems, adaptive focusing techniques mimicking optical phase aberration corrections used in astronomy have been implemented that correct only for phase distortion [61–70]. They assume that the inhomogeneities, mainly attributed to the abdominal wall, are modelled as a thin region where the sound velocity is different from that of the remaining tissues and that this random layer is located in the very near-field of the transducer array. The great simplification due to this model is that, because the time shifting layer is located close to the probe, its effects can be faithfully described as adding a random

aberrating time delay law to the classical beamforming delays. Improvements of the image quality rely on the use of transducer arrays driven with an appropriate focusing time delay law that compensates the unknown time shifts induced by the random phase screen. They reduce to an automatic estimation of the proper time delay law. Several techniques have been proposed for this estimation. After an initial insonification of the region of interest, the echoes from a reflective target or from a scattering medium are received by a transducer array. In a technique proposed by O'Donnell [63,64], the received signals are cross-correlated and the time delays are determined by the time shift corresponding to the maximum of the cross-correlation between signals from neighbouring transducer elements. Another time delay estimation technique using speckle brightness as a quality factor has been investigated by Trahey [65,66]. These methods are also valid if a randomly scattering medium is available in the field of interest, instead of a pointlike reflector. In this case the methods are based on the fact that scattering media give correlation between signals received on adjacent array elements. The correlation structure in speckle data can be studied by the Van Cittert–Zernike theorem, that was applied to pulse echo ultrasound by Fink *et al* [67,68].

Although these techniques are attractive, the experimental results observed *in vivo* are in many cases disappointing. They suffer from the lack of validity of the assumed model of a thin random phase screen close to the array. Indeed in many situations, the acoustic inhomogeneities are not located near the array, but are distributed in the whole volume, invalidating the assumption of a near-field random phase. A wave originating from a point scatterer and propagating in such an inhomogeneous medium is not only delayed: the spatial and temporal shape of the wave is also distorted through refraction, diffraction and multiple scattering. Steinberg *et al* [69,70] show, for very-narrowband point source illumination, that the wavefront distortion due to breast tissue is not only described by a phase distortion but also by an amplitude distortion. Other accurate measurements of waveform distortion made by Waag *et al* [71,72] also show a strong amplitude modulation due to the abdominal wall and even some multiple scattering effects due to connective tissues. Time delay techniques can compensate only for phase distortions. Amplitude compensation of the signal is also needed in order to correct for the amplitude distortion. However, with broadband signals such as those used in pulsed mode, each spectral component of the wavefront is subjected to different phase and amplitude distortions. In such a case, optimal focusing cannot be achieved for pulsed signals with only delay line techniques and simple amplitude modulation on the aperture.

Optimal focusing requires one to take into account all the information received on the array from the point source. For a monochromatic signal, this information corresponds to the amplitude and phase modulations on each transducer element. For a pulsed signal, all the individual received waveforms need to be taken into account. For each scatterer in the medium of interest, a matched filter must be designed to compensate all the distortions of the wavefront.

TR and phase conjugation techniques [1, 73, 74] provide a means to find this matched filter. The TR method corrects for phase, amplitude and even shape aberrations and thus is more efficient than time shift compensation techniques. However, it is an optimal technique only when dissipation is negligible. It also requires, as a first condition, the presence of one dominant scatterer in the region of interest. To make an ultrasonic image of the zone surrounding the dominant scatterer, one has to focus not only on the dominant scatterer, but also around it in order to map the reflectivity of the surrounding zone. For this purpose, different algorithms have been developed to modify the initial matched filter to obtain the set of matched filters corresponding to each point of the zone of interest [75].

When the medium of interest does not contain a dominant scatterer but only a random distribution of scatterers, the TR technique does not work and further improvements are necessary before it can be applied to this kind of medium, which is frequently encountered in

medical imaging. However, for therapeutic uses such as lithotripsy, the goal is to focus a beam on a kidney stone which behaves as the dominant scatterer in the region of interest. Likewise for hyperthermia or ablathermia, invasive methods using implantable acoustic sensors inside tumours for acoustic feedback have been proposed [76].

In the next sections, we present two medical applications of TRMs. The objective is to focus high-power ultrasound beams through heteregoneous media for non-invasive local destruction of kidney stones or malignant tumours. Although the location of the target may be accurately determined with x-ray or NMR systems, accurate focusing of an ultrasonic wave through heterogeneous tissue is not guaranteed. For a stone or tumour located in the abdomen, a crucial problem is motion due to patient breathing. Indeed, the amplitude of the resulting movement can be as large as 2 cm and tracking the target is requirerd for an efficient therapy.

5.1. Time reversal focusing applied to lithotripsy

The main problem to overcome in the field of lithotripsy is related to stone motion due to breathing. The lateral dimension of the shock wave in current lithotripsy devices is less than 5 mm, and amplitude of stone displacement can reach up to 20 mm from the initial position. Hence, many shock waves miss the stone and submit neighbouring tissues to shocks that may cause local bleeding.

Different approaches have been investigated to overcome these limitations. Most of them are based on a trigger of the high-power pulses when the stone goes through the focus of the shock wave generator. These approaches may reduce the number of shots needed to disintegrate the stone but considerably increase the time of treatment. A TR piezoelectric generator has been developed [77] to electronically move the focus and track the stone during a lithotripsy treatment.

The goal is to locate and focus on a given reflecting target among others as, for example, a stone surrounded by other stones and organ walls. Moreover, the stone is not a pointlike reflector but has dimensions up to ten times the wavelength. In the basic procedure that has been developed, the region of interest is first insonified by the transducer array. The reflected field is received on the whole array, time reversed and retransmitted. As the process is iterated, the ultrasonic beam selects the target with the highest reflectivity. If the target is spatially extended, the process converges on one spot, whose dimensions depend only on the geometry of the TRM and the wavelength. High amplification during the last iteration can be used to produce a shock wave for stone destruction. However, two problems limit this technique. For human applications, it is necessary to use very short high-power signals to prevent damage caused in the organs by cavitational gas bubbles, while the iterated pulses have long duration. In addition, a complete TR apparatus is expensive and the number of TR channels must be limited. To solve these problems, another procedure has been developed. In the first step, only a subgroup of the array is used in a time-reversed mode. This step is conducted with low-power ultrasound in order to remain in linear acoustics. After several iterations, a low-power ultrasonic beam, generated by the array subgroup, is focused on the stone. The last set of received signals are used to deduce a time-of-flight profile on the subgroup. This time-of-flight profile is then interpolated to the whole array. The final step consists in the generation, by the whole array, of very short high-power signals with the correct delays.

TR experiments are performed with a probe made of a bidimensional transducer array working at a central frequency of 360 kHz, especially designed for lithotripsy. The probe is made of 121 prefocused piezo-composite transducer elements arranged on a spherical cup of 190 mm radius of curvature (see figure 37). To illustrate the efficacy of the TR approach, two focusing experiments are presented in the following. The first is conducted on a gallbladder stone

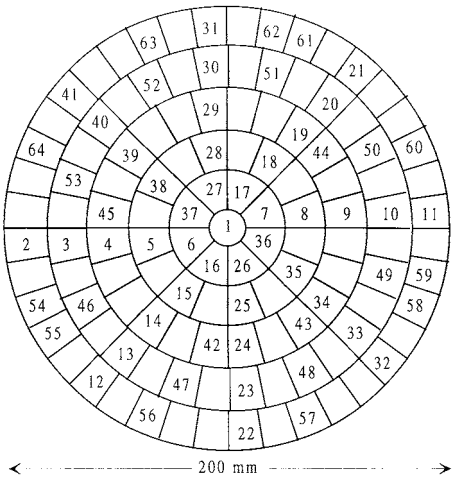

Figure 37. Geometry of the prefocused two-dimensional TRM developed for lithotripsy. The connected elements are numbered.

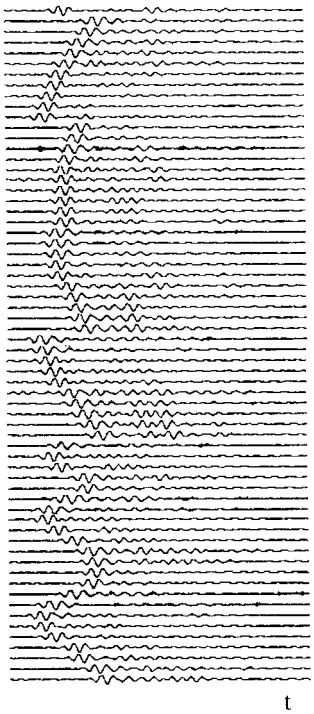

Figure 38. Echographic signals recorded from a gallbladder stone after the first illumination.

of approximately spherical shape. The other deals with a large kidney stone of irregular shape.

In the gallbladder experiment, the stone has a diameter of 18 mm, much larger than the ultrasonic wavelength of 4 mm. The stone is immersed in a water tank at a depth $z = 170$ mm from the surface of the array and at position $x = 10$ mm, $y = 20$ mm off-axis. In the first step, a pulse is transmitted by a single transducer element located in the centre of the array. The echoes from the stone are recorded by a subgroup of 64 transducers (figure 38). Each line is normalized in the display and the 64 signals are presented from channel 1 to channel 64. On each channel, the first echo comes from the specular reflection on the surface of the stone. These signals have the same temporal shape. They line up according to a wavefront characterizing the location of the stone. Approximately 10 μs after this signal, a second echo is observed on several channels corresponding to a creeping wave or to a secondary diffraction on the back side of the stone.

In the second step, the stone is removed and the recorded signals are time reversed and retransmitted. The time-reversed wave propagates and the resulting pressure pattern is measured with a hydrophone in the plane of the stone (figure 39). We observe that the pressure field is focused on a bright point of the stone. Indeed, the -6 dB beam width is equal to 5.9 mm, which is the dimension of the array point spread function at this location whereas the stone diameter is about 18 mm. Thus, the TR process has focused the beam on a spot whose dimensions depend only on the geometry of the array and the location of the stone.

In order to explain such focusing on a small portion of an extended target, we take into account only the specular echoes whose amplitudes are much higher than those resulting from the elastic response. From the scattering point of view, the target shell may be considered

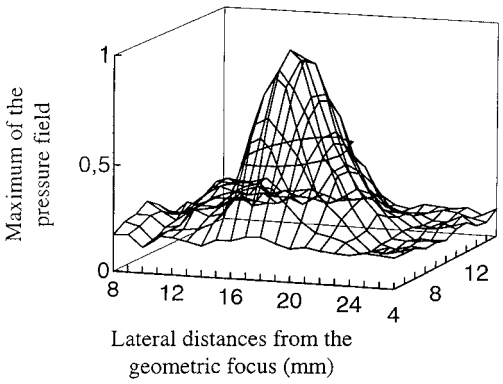

Figure 39. Directivity pattern (maximum of the pressure field) measured in the plane of the gallbladder stone, $z = 170$ mm. The 64 transducers transmit simultaneously the time-reversed signals of figure 2.

as a continuous set of target points of different scattering strengths. The first backscattered wavefront results from the interference pattern of the waves scattered by each surface element of the stone. One of these surface elements yields a significant echo only if the wavelets scattered in its region interfere constructively on the surface of the transducer array. Such a bright point is located on a surface element for which the acoustic path is an extremum (stationary phase theorem).

The stone has a spherical shape and a surface roughness which is very small compared with the ultrasonic wavelength (4 mm). In the case of an initial illumination with a single element, there is only one bright point for each receiving element. Moreover, a simple geometric analysis shows that all these bright points are located on a surface of dimensions equivalent to a disc of diameter 5 mm. Thus, the wavefront backscattered by this stone comes from a small region whose dimension is about one wavelength. This experiment shows that even in the case of an extended target, the TR process selects the brightest point of its surface and the resulting beam focuses on a spot with dimensions of the order of the diffraction point spread function.

The second experiment is performed with a kidney stone of very large dimensions (approximately $x = 30$ mm, $y = 20$ mm and $z = 20$ mm). This stone is much larger than the previous one and its shape has irregularities of the size of the wavelength. It has several bright points and iteration of the TR process is needed to obtain a sharp focus. The stone is located near the geometrical focus of the probe and a pulse is transmitted by a single element located at the centre of the array. After the first illumination, echoes from the stone are recorded by the 64 connected transducers (figure 40(a)). We observe that the shape of the signal can be very different from one transducer to the other. There are several bright points on the surface of the stone and the waves reflected by them interfere in the plane of the array. Moreover, elastic responses are higher than in the previous experiment.

At this step, the TR process is iterated and the corresponding wavefronts recorded. Figure 41 shows the directivity patterns along an axis parallel to both the array aperture and the greatest dimension of the stone. The directivity pattern corresponding to the first iteration confirms that the wave detected on the array comes from several bright points. There is one main lobe (whose dimensions correspond to the diffraction point spread function) and two side-lobes. On the next iteration, the side-lobe level decreases significantly, but after four iterations it remains relatively high. These bright points have a similar reflectivity and hence many iterations are required to select the brightest one.

To optimize the side-lobe level, an algorithm, valid for an homogeneous medium, has been implemented. First, the time of flight between the bright point selected by the iterative TR process and each transducer is determined. A classical method to determine the arrival time of

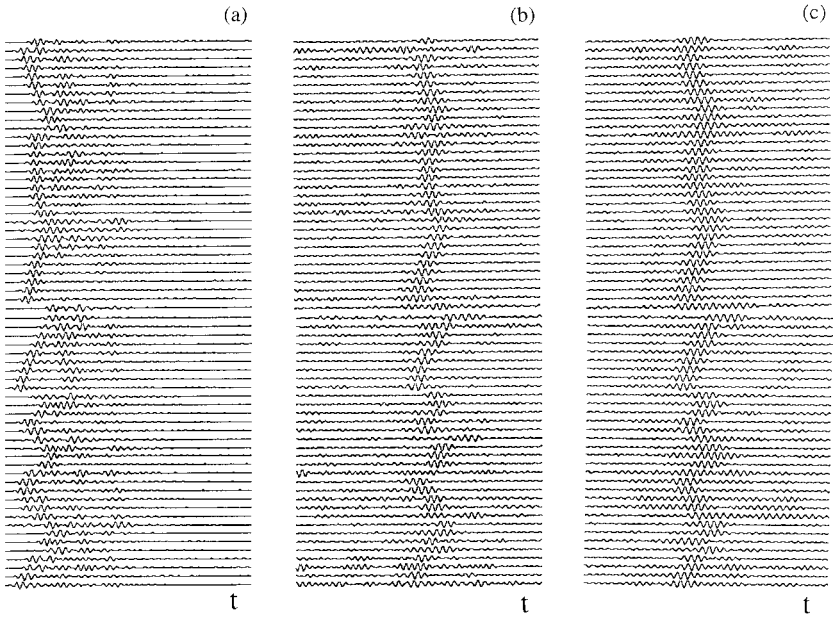

Figure 40. Echographic signals recorded from a kidney stone after (*a*) the initial illumination, (*b*) the second and (*c*) the fifth iteration of the TR process.

echoes from a pointlike reflector is to use cross-correlation between signals from neighbouring transducer elements. However, for a complex target like a stone, the spatial coherence of the backscattered wave can be very limited. Indeed, as seen in the previous experiment, specular echoes from an extended target may result from the interference of wavelets coming from several bright points and thus be very different from one element to another. Moreover, depending on the transducer element, one or two replicas of the specular echo can be observed (figure 40(*a*)). The accuracy with which these arrival times can be estimated is then limited by the degree of correlation between received signals. The iterative TR process behaves as a spatial filter which selects the brightest surface element and hence improves the level of coherence across the array (figure 40(*c*)). The calculation of the relative times of flight between signals using the cross-correlation technique is time consuming. The TR process achieves an analogous correlation between the inter-element impulse–response [77] and thus the offset of the peak in the signals measured after a TR operation gives a much faster determination of the arrival times.

Finally, this set of experimental time delays is fitted with a spherical model that depends on the unknown spatial coordinates, x, y, z, of the bright point. The medium of propagation is assumed to be homogeneous (distortion due to refraction in tissues is very weak at 360 kHz). The estimated coordinates are used to steer a very short beam. The focusing obtained on the one hand with the iterative TR process and on the other hand with time-shifted pulses (according to the estimated coordinates) can now be compared (figure 42). Both acoustic beams focus at the same location and that the algorithm improves spatial filtering: the main lobe is sharper and the secondary lobe has been eliminated. Moreover, the time delay profile can be now interpolated to the 121 transducers, which allows the generation of the high-power ultrasound beam from the whole array. Another advantage of this optimization method is to provide controls on the process. First, the tracking area can be limited and the shock wave

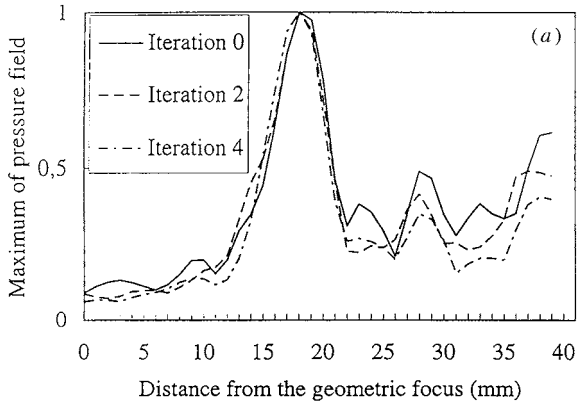

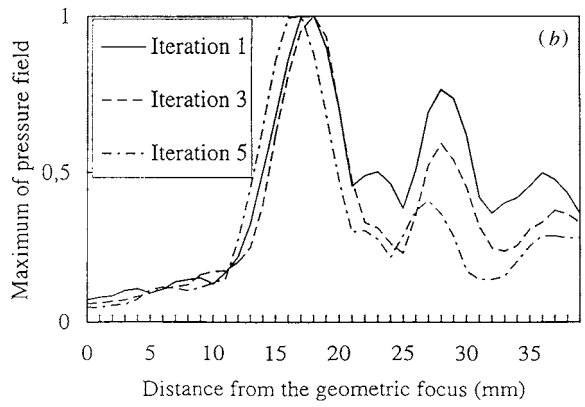

Figure 41. Directivity patterns along the y axis at (*a*) iterations 0, 2, 4 and (*b*) iterations 1, 3, 5.

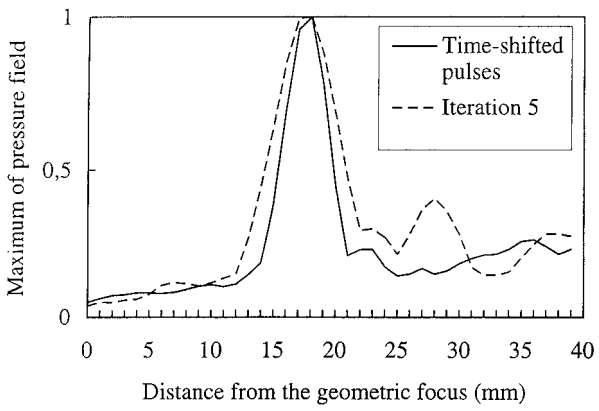

Figure 42. Comparison of the directivity patterns along the y axis obtained with the TR process and pulses time shifted according to the estimated coordinates.

triggered only if the estimated location of the stone is in the region defined by the physician. Second, the quality of the match between the time-shifting law and a spherical model provides a way to assess whether the echoes come from one bright point.

A prototype especially designed for TRM experiments in the field of lithotripsy has been developed [77]. It is able to determine the coordinates of one bright point of the target in less than 40 ms within a region of 60 mm along the axis and 40 mm laterally. Many *in vitro*

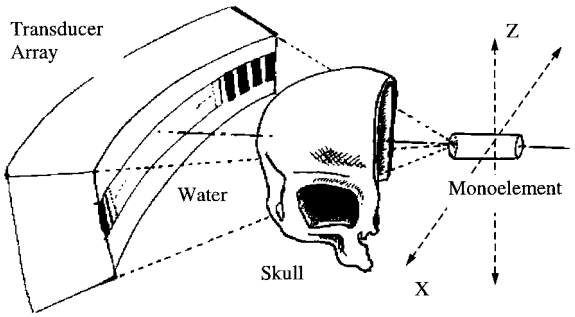

Figure 43. Experimental setup.

experiments with kidney or gallbladder stones have shown the efficiency of the method. *In vivo* experiments have been performed, yielding very encouraging results.

5.2. Medical hyperthermia and brain therapy: focusing in dissipative media

Another major promise of self-focusing TRM arrays that has not yet been completely fulfilled is ultrasonic medical hyperthermia. In this technique, high-intensity ultrasonic energy is absorbed by the tissue and converted to heat, resulting in an increase in local temperature. If local temperature rises above 60 °C, tissue destruction can occur within seconds. Focused ultrasound surgery, pioneered in the 1950s by Fry at the University of Illinois, has not gained general acceptance until recently. Focal probes consisting of annular phased arrays are now marketed for the treatment of prostate cancer. These techniques are limited to the production of necrosis in tissues that are not moving: application to abdominal and cardiac surgery is limited by the tissue motion induced both by the cardiac cycle and by breathing. At the University of Michigan, Ebbini and his group are developing self-focusing arrays to solve this problem [76]. In our group, we are working on TRM techniques applied to brain hyperthermia. The challenge of this application is to focus high-power ultrasound beams through the skull for local destruction of malignant brain tumours. However, the skull induces severe refraction and scattering of the ultrasonic beam, and moreover, the porosity of the skull produces a strong dissipation that breaks the TR symmetry of the wave equation. It has been shown [78, 79] that TR focusing is no longer appropriate to compensate for the properties of the skull and a new focusing technique has been developed that combines a correction of the dissipative effects with classical TR focusing. In a first step, this technique allows one to focus on an artificial source implanted inside the treatment volume during the NMR guided biopsy. In a second step, the ultrasonic beam is steered on points surrounding this beacon in order to investigate and burn the whole volume of the tumour.

Experiments are conducted with a 1D prefocused cylindrical array of transducers made of 128 piezoelectric elements working at a central frequency of 1.5 MHz ($\lambda = 1$ mm). A dried human skull has been cut in the midsagittal plane and stored in a water tank. The skull is located between the source and the array of transducers and the array is about 40 mm away from the skull (figure 43). Figure 44 shows the directivity patterns of the focused beams in three different cases. First a reference pattern is obtained through water with cylindrical focusing (grey curve). Introducing the skull induces a severe defocusing of the cylindrical beam (dashed curve): the beam is widely spread. However, the result obtained with TR focusing is also poor (solid curve). This figure shows that TR focusing is slightly better but remains far from the optimum. In order to understand this behaviour, the wavefront, coming from the source and recorded by the 128 transducers, is presented in greyscale in figure 45. Not only can we

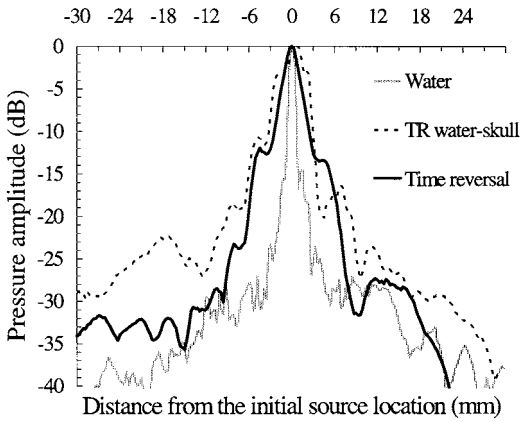

Figure 44. Directivity patterns obtained by TR through pure water (grey curve), focusing through the skull assuming a homogeneous medium (dashed curve) and TR through the skull (solid curve).

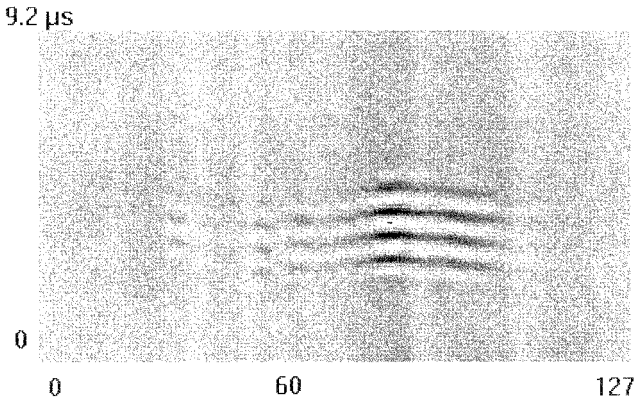

Figure 45. Waveforms received through the skull.

observe a phase distortion of the wavefront, but a strong amplitude modulation is also visible. In this experiment, the amplitude modulation is mainly due to absorption losses that occur in the skull and cannot be compensated by the TR operation. Indeed, the transducer elements located in front of a strongly absorbing region receive and transmit after the TR operation a signal of small amplitude. Thus, when the wavefront goes back through the aberrating layer, the amplitude modulation is in fact squared.

From a mathematical point of view, the TR focusing method is related to the invariance of the wave equation under the change of t to $-t$. However, acoustic losses are taken into account in the wave equation by a first-time derivative and are no longer TR invariant. Indeed, one way to introduce losses is to modify the equation of state to allow for a delay between the application of a sudden pressure change and the attainment of the resulting deformation [54]. This modification yields a third term in the wave equation for an absorbing fluid medium:

$$\left(L_r + L_t + \frac{\tau(\vec{r})}{\rho(\vec{r})}\partial_t \vec{\nabla}\left(\frac{1}{\rho(\vec{r})}\vec{\nabla}\right)\right) p(\vec{r}, t) = 0 \tag{49}$$

where τ is the relaxation time.

In order to improve the TRM focusing, a first pretreatment that takes into account the amplitude modulation due to absorption can be added. If we assume that the skull can be modelled as a thin random absorbing phase screen located close to the array, the amplitude

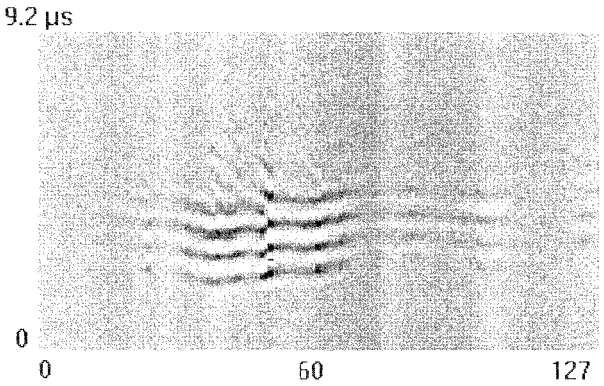

Figure 46. Waveforms received through the skull after amplitude compensation.

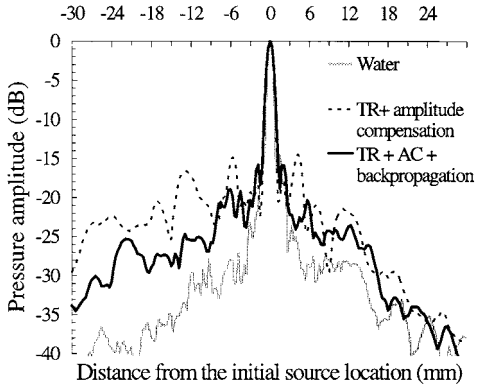

Figure 47. Directivity patterns obtained by TR through pure water (grey curve), TR with amplitude compensation in the aperture (dashed curve) and TR with amplitude compensation after backpropagation (solid curve).

modulation is only due to absorption losses. The amplitude modulation is estimated by comparison with a reference waveform obtained in the same condition in a homogeneous medium. This estimation is used to invert the amplitude modulation of the wavefront. Figure 46 shows the wavefront after this amplitude compensation. Then, the compensated wavefront is time reversed and transmitted. The corresponding directivity pattern is plotted on figure 47 (dotted curve). The amplitude compensation improves focusing, and the beamwidth is perfectly corrected up to -14 dB below the peak. However, in real experiments this compensation is not optimal. Indeed, due to mechanical and thermal problems, the array is located in the water tank at 40 mm from the skull. The wavefront, coming from the source, after passing through the skull, has to propagate towards the array at 40 mm water depth. During this step, new phase and amplitude modulations are added. These effects are automatically compensated by the backpropagation of the time-reversed wavefield and need not be taken into account a second time in the pretreatment. To improve the focusing process, the amplitude compensation must be applied only to the amplitude distortion due to acoustic losses in the skull. For this purpose, amplitude distortion developed during propagation from the skull to the receiving aperture can be reduced by a numerical TR operation. This numerical backpropagation of the received wavefront toward the aberrating layer is similar to the one presented by Fink and Dorme [73, 75], and uses the Green function of the homogeneous medium. Thus, the original diverging wavefront recorded by the array is first backpropagated numerically from a cylindrical surface with radius 100 mm to one with radius 60 mm, corresponding respectively

to the array aperture and the skull surface. Amplitude distortion is then estimated along the skull surface. An amplitude-compensated waveform is then computed on this surface and numerically backpropagated from the skull to the array. Thus, a new set of 128 signals matched to the initial source location are computed. These signals are time reversed and transmitted in the medium. Figure 47 shows a comparison of the focusing results obtained with amplitude compensation in the aperture (dashed curve) and amplitude compensation after backpropagation (solid curve). The main improvement is on the side-lobe level, which is -12 dB below the main peak level. Note that in this study, a 1D array is used. Since significant aberration exists both in elevation and azimuth, aberration correction should be performed in both dimensions to be most effective. Nevertheless, this focusing quality seems quite good for hyperthermia, where the heating pattern is proportional to the ultrasound energy. This experiment emphasizes the difference between TR and matched filter, because the spatial reciprocity theorem holds even in the case of an absorbing medium. Therefore the matched filter theory implies that each individual transducer contribution reaches its maximum at the same time T at the source location, allowing a constructive interference. But this theorem does not predict anything about the pressure obtained at other locations and times. An amplitude compensation combined with the TR method is required to improve focusing.

Although amplitude compensation and TR allow self-focusing on an artificial source implanted inside the treatment volume, the beam has to be steered at points surrounding this beacon to treat a tumour. In homogeneous media, conventional beamsteering consists in tilting the wavefront focused on the artificial source. This can be obtained by delaying the pulses according to a 'tilt' delay law. In heterogeneous media, this process is only valid for small angles or when aberrations are located close to the array. Indeed, this angle depends on the coherence length of the aberrating layer and on its position with respect to the array (this problem is equivalent to the determination of the isoplanetic angle in astronomy). Nevertheless, numerical backpropagation allows one to extend this method to aberrating layers located at any distance from the array [50]. The process is applied at 5, 10 and 15 mm away from the initial source location. Figure 48 shows a comparison of the oblique directivity patterns obtained in three cases. The grey curves shows the effect of tilting the wavefront in water only by delaying the signals with an oblique law. The dashed curves show, in presence of the skull, the effect of both tilting and amplitude compensation of the wavefront in the array aperture and the solid curves show the results obtained by tilting and amplitude compensation of the wavefront after numerical backpropagation to the skull. Without backpropagation, the focusing is quickly degraded as the distance from the initial source location increases; thus, side-lobes appear respectively at -12 dB, -6 dB and -2 dB. On the other hand, the focusing remains quite good when backpropagation to the skull array range is applied before amplitude compensation and tilting of the wavefront. Side-lobes appear respectively at -12 dB, -12 dB and -14 dB. Conventional beamsteering that consists in tilting the wavefront without backpropagation is no longer effective when the aberrating and absorbing layer is located far away from the transducer array.

These results clearly show the possibility of controlling the shape of an ultrasonic beam through the skull on a large region surrounding an artificial source. Recently Hynynen has developed a phased array technique, without amplitude correction, to focus through the skull [80].

6. Nondestructive evaluation with TRM

Another important application of TRM is flaw detection in solids. The detection of small defects is difficult when the inspected object consists of heterogeneous or anisotropic material and when the sample has complex geometry. Usually, the solid and the ultrasonic transducers are immersed in water, and the transducers are moved to scan the zone of interest. Due to refraction, the ultrasonic beams can be altered by the water/solid interface. Furthermore,

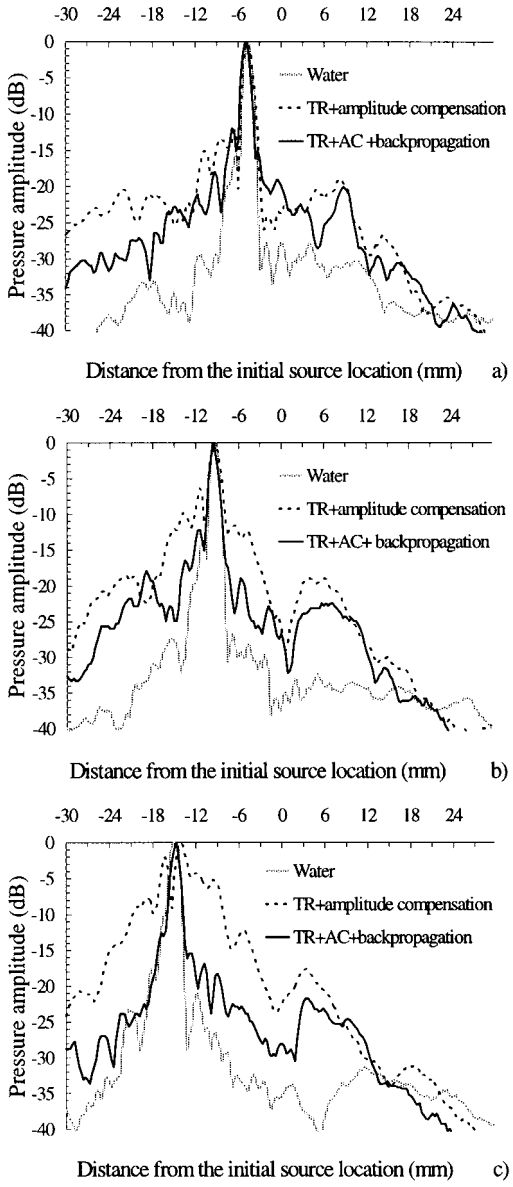

Figure 48. Directivity patterns obtained by tilting the wavefront received from the initial point source at a distance of (*a*) 5 mm, (*b*) 10 mm and (*c*) 15 mm: tilting through pure water (grey curves), TR of the signal received through the skull with amplitude compensation (dashed curves), TR of the amplitude compensated signal after backpropagation (solid curves).

the longitudinally polarized ultrasound travelling in water produces waves of different polarizations and velocities in the solid which can support transverse and surface waves. Because of refraction and acoustic mode conversion, a spherical piezoelectric transducer immersed in water produces several acoustic beams in the solid, and each beam poorly converges to a different focal point. To solve this problem, a transducer with a surface geometry (Fermat surface) adapted to a particular focal point is sometimes manufactured. The transducer geometry is such that the waves emitted from each point on the transducer surface arrive simultaneously at the focal point and interfere constructively. This technique is problematic for thick samples for which many transducers of varying geometries must be available to scan through the volume of interest. Step-by-step scanning of a sample using these

transducers is more time consuming as focusing is improved.

The use of ultrasonic arrays with electronic focusing and steering capabilities seems an interesting solution for real-time inspection. However beam focusing and steering of the ultrasonic array in the solid is a difficult task for which self-focusing techniques have been proposed to enhance the flexibility of the process [56]. Using TRMs is a very effective technique to solve these problems. TRMs automatically compensate for refraction, mode conversion and anisotropy. Another very attractive feature of TR processing is its speckle noise reduction capability. Indeed, if the speckle noise results from random microstructure whose scale is less than the wavelength, the TR process cannot exactly refocus on the speckle noise sources. Each individual scatterer gives a time-reversed wave that focuses back on it with a diffraction spot but the interference between all these spots gives a complicated pattern that does not match the exact scatterer distribution. Using this property, processing techniques have been developed that allow one to distinguish, during the inspection, a low-contrast flaw from high-level incoherent speckle noise.

A 128-element TRM has been built to detect the presence of low-contrast defects within titanium alloys used in jet engines. Figure 49 shows results obtained with a TRM made of 128 real-time channels by Wu *et al* [57, 58]. The geometry of the piezoelectric matrix is similar to that in figure 35, except that the probe diameter is 60 mm and the centre frequency is 5 MHz. The goal was to detect the presence of low-contrast hard-α defects within these titanium alloys. A hard-α defect is a localized region of grains which have a substantially higher hardness and brittleness than the surrounding material. If not detected, hard-α inclusions can become crack initiation sites, and lead to component failure. Hard-α detection is a difficult problem because titanium has a highly heterogeneous microstructure which produces large amounts of scattering noise that can hide the echo from a hard-α defect.

To find the defects, the TRM array and a titanium sample containing different defects mimicking hard-α are immersed in water facing each other. The titanium sample is first illuminated using the central part of the transducer array and the echoes are recorded by the whole array. In this experiment the incident beam is only converted into a longitudinal wave propagating in the titanium (the speckle noise is weaker for longitudinal than for shear waves in titanium). In figure 49(*a*) the signals coming from a region containing a low-contrast defect are shown using a greyscale code. The echoes from the two titanium/water interfaces are clearly visible. Between these two echoes, we can observe the speckle noise caused by the titanium microstructure but the echo from the defect is hidden by the high level of speckle noise. A portion of the acoustic signal is then selected using a time window, time reversed, and re-emitted by the whole array. The new backscattered signals then show a completely different behaviour: a well contrasted wavefront appears in the window range (figure 49(*c*)). Although the defect is located 5 mm off-axis of the transducer array, the TR procedure refocuses the acoustic energy on this defect and thus its backscattered energy increases considerably. The wavefront phase modulation corresponds to the wave backscattered by the defect which reaches the 2D array with oblique incidence. Figures 49(*b*) and (*d*) show the signal resulting from the summation of all the signals of figures 49(*a*) and (*c*), respectively. A signal-to-noise ratio improvement exceeding 20 dB is observed between the first and the second illumination. The same experiment conducted in a pure speckle zone would give a very different behaviour: two different noise echo patterns would be observed after each illumination because the illuminated beams are different and the summation operation described earlier would give a weak signal.

Although this technique gives impressive results, it reduces only to self-focusing in transmit mode and a better signal-to-noise ratio may be obtained by also focusing in the receive mode. The summation of the received signals that we described earlier is not very

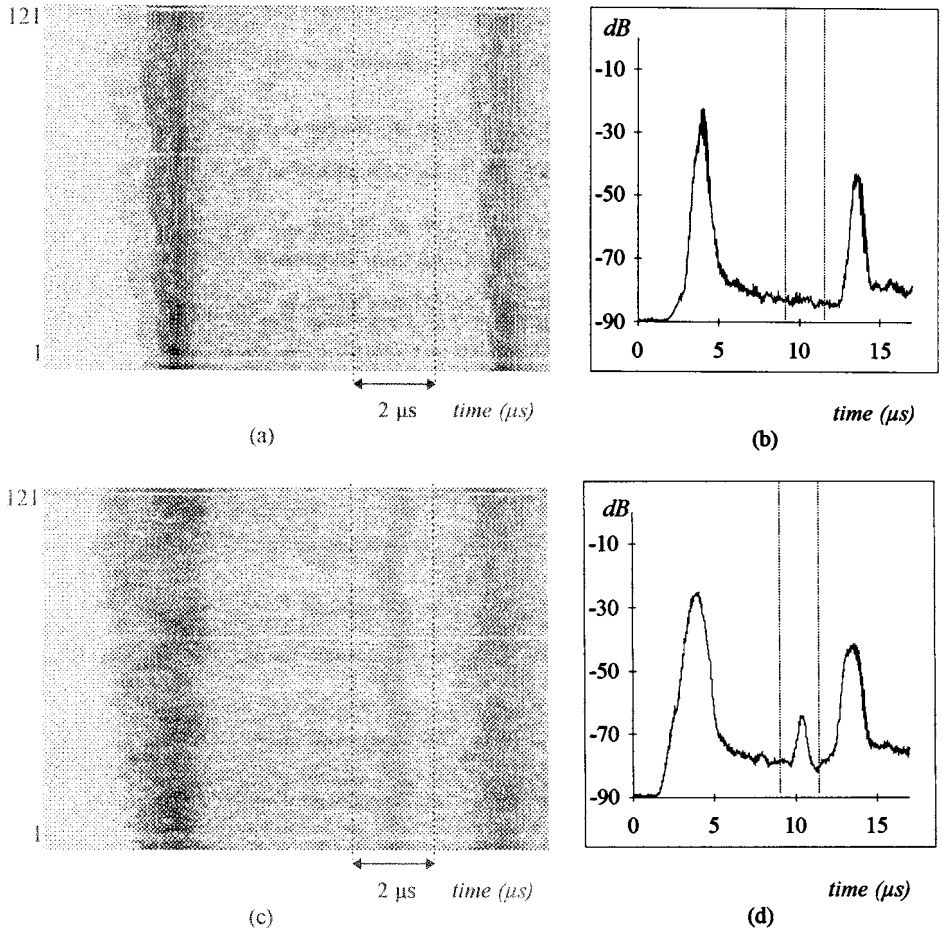

Figure 49. (*a*) Bscan presentation of the 121 backscattered signals received after a first illumination from a hard-α defect located 5 mm off-axis. (*b*) The summation of the received signals from all the transducer elements (0–90 dB). (*c*) Bscan presentation of the backscattered signals after one TR operation. (*d*) The summation of the signals from (*c*) shows an improvement of the signal to noise of 20 dB.

effective. We have to compensate for the different time delays between the array elements and the defect before the summation. But the estimation of the delays only has to be done if the window contains a defect. Indeed, we must be very careful when we estimate the delays in a speckle-only window. To be certain that the estimated delays cannot increase the speckle noise, we use a trick that consists of a second TR operation. Indeed, if the initial window selects the echo of a defect, the signals received after the second iteration always contains the same wavefront, with the same phase modulation (the wavefront is an invariant of the TR operation). If the window contains only speckle noise, the *second iteration* gives a different noise pattern. An automatic determination of the delay law is then made at the *second iteration* by measuring the arrival time of the peak signal on each channel. Once this delay law is determined it is use to compensate the signals received at *first iteration*. If the window selects a defect, the *second iteration* delay law is then optimized to compensate the signals from the *first iteration*, but if the window selects speckle noise the *second iteration* delay law does not match the signals of

the *first iteration* and the summation is ineffective. It is as if one introduced a random phase screen before the summation.

The iterative pulse echo mode allows one to autofocus and to detect defects as small as 0.3 mm in 250 mm diameter titanium billets. Compared with other techniques, the signal-to-noise ratio is enhanced in all situations, and smaller defects can be detected in the billet core where ultrasonic beams are strongly distorted. Various applications of TRMs are now under investigation such as, for example, crack detection in parts of nuclear reactors made of large-grain anisotropic austenitic steel.

Conclusion

TR shows startling applications in the field of acoustics. Because acoustic TR technology is now easily accessible to modern electronic technology, it is expected that applications in various areas will expand rapidly. Initial applications show promise in medical therapy as well as in nondestructive testing. Underwater detection and telecommunications are also important areas of interest. In addition to solving practical problems, TRMs are unique research tools that may allow us to better understand problems related to wave propagation in complex static or dynamic media. They may be used to study inverse scattering problems, multiple scattering processes and chaotic scattering as well as scattering by turbulent media.

References

[1] Fink M, Prada C, Wu F and Cassereau D 1989 Self focusing in inhomogeneous media with time reversal acoustic mirrors *Proc. IEEE Ultrasonics Symp. (Montreal)* vol 1 pp 681–6

[2] Fink M 1992 Time reversal of ultrasonic fields: basic principles *IEEE Trans. Ultrason. Ferroelec. Freq. Contr.* **39** 555–66

[3] Fink M 1997 Time-reversed acoustics *Phys. Today* **50** 34–40

[4] Jackson D R and Dowling D R 1991 Phase conjugation in underwater acoustics *J. Acoust. Soc. Am.* **89** 171

[5] Cassereau D and Fink M 1992 Time reversal of ultrasonic fields: theory of the closed time reversal cavity *IEEE Trans. Ultrason. Ferroelec. Freq. Contr.* **39** 579–92

[6] Porter R P and Devaney A J 1982 Generalized holography and the inverse source problems *J. Opt. Soc. Am.* **72** 327–30

[7] Cassereau D and Fink M 1994 Time reversal focusing through a plane interface separating two fluids *J. Acoust. Soc. Am.* **96** 3145–54

[8] Kino G S 1987 *Acoustics Waves (Signal Processing Series)* (Englewood Cliffs, NJ: Prentice-Hall)

[9] Zel'dovich B Ya, Pilipetsky N F and Shkunov V V 1985 *Principles of Phase Conjugation* (Berlin: Springer)

[10] Pepper D M 1988 Nonlinear optical phase conjugation *Laser Handbook* vol 4 (Amsterdam: North-Holland) pp 333–485

[11] Vlasov D V, Zabolotskaya E A and Kravtsov Yu A 1983 Acoustic phase conjugation in water containing bubbles *Sov. Phys. Acoust.* **29** 69–70

[12] Zabolotskaya E A 1984 Phase conjugation of sound beams in connection with four-phonon interaction in a liquid containing gas bubbles *Sov. Phys. Acoust.* **30** 462–3

[13] Sato T, Kataoka H, Nakayama T and Yamakoshi Y 1989 Ultrasonic phase conjugator using micro particle suspended cell and its application *Acoustical Imaging* vol 17 (New York: Plenum) pp 361–70

[14] Bunkin F V, Vlasov D V, Zabolotskaya E A and Kravtsov Yu A 1983 Phase conjugation of sound beams in four-phonon interaction with temperature waves *Sov. Phys. Acoust.* **28** 440–1

[15] Yanase T, Watanabe Y and Urabe Y 1995 Acoustic phase conjugation mirror using microcapsules *J. Acoust. Soc. Japan* **51** 221–6 (in Japanese)

[16] Shiren N S, Melcher R L and Kazyaka T G 1986 Multiple-quantum phase conjugation in microwave acoustics *IEEE J. Quant. Electron* **22** 1457–60

[17] Thompson R B and Quate C F 1971 Nonlinear interaction of microwave electric fields and sound in $LiNbO_3$ *J. Appl. Phys.* **42** 907–91

[18] Nelson D F 1978 Three-field electroacoustic parametric interactions in pi-ezoelectric crystals *J. Acoust. Soc. Am.* **64** 891–5

[19] Ohno M 1989 Generation of acoustic phase conjugate waves using nonlinear electroacoustic interaction in $LiNbO_3$ *Appl. Phys. Lett.* **54** 1979–80
[20] Ohno M and Takagi K 1996 Enhancement of the acoustic phase conjugate reflectivity in nonlinear piezoelectric ceramics by applying static electric or static stress fields *Appl. Phys. Lett.* **69** 3483–5
[21] Ohno M, Yamamoto K, Kokubo A and Takagi K 1999 Acoustic phase conjugation by nonlinear piezoelectricity I. Principle and basic experiments *J. Acoust. Soc. Am.* **106** 1330–8
[22] Brysev A P, Bunkin F V, Vlasov D V, Krutianskii L M, Preo-brazhenskii V L and Stakhovskii A D 1989 Parametric phase conjugation of an ultrasonic wave in a ferrite *Sov. Phys. Acoust.* **34** 642–3
[23] Krutiansky L M, Preobrazhensky V L, Pyl'nov Yu V, Brysev A P, Bunkin F V and Stakhovsky A D 1992 Observation of ultrasonic waves in liquid under overthreshold parametric phase conjugation in ferrite *Phys. Lett.* A **164** 196–200
[24] Brysev A P, Krutyanskii L M and Preobrazhenskii V L 1998 Wave phase conjugation of ultrasonic beams *Sov. Phys.–Usp.* **41** 1–13
[25] Nikoonahad M and Pusateri T L 1989 Ultrasonic phase conjugation *J. Appl. Phys.* **66** 4512–3
[26] Derode A, Roux P and Fink M 1995 Robust acoustic time reversal with high order multiple scattering *Phys. Rev. Lett.* **75** 4206–9
[27] Snieder R and Scales J 1998 Time-reversed imaging as a diagnostic of wave and particle chaos *Phys. Rev.* E **58** 5668–75
[28] Derode A 1994 *PhD Thesis* Paris 7 University
[29] Derode A, Tourin A and Fink M 1999 Ultrasonic pulse compression with one-bit time reversal through multiple scattering *J. Appl. Phys.* **85** 6343
[30] Roux P, Roman B and Fink M 1997 Time reversal in ultrasonic waveguide *Appl. Phys. Lett.* **70** 1811–3
[31] Parvulescu A 1995 Matched-signal (PESSS) processing of the ocean *J. Acoust. Soc. Am.* **98** 943–60
[32] Parvulescu A and Clay C S 1965 Reproductibiity of signal transmission in the ocean *Radio Elect. Eng.* **29** 233
[33] Feuillade C and Clay C S 1992 Source imaging and side-lobe suppression using tie-domain techniques in a shallow-water waveguide *J. Acoust. Soc. Am.* **92** 2165–72
[34] Kupperman W A, Hodgkiss W S, Song Hee C, Akal T, Ferla C and Jackson D 1998 Phase conjugation in the ocean: experimental demonstration of an acoustic time reversal mirror *J. Acoust. Soc. Am.* **103** 25–40
[35] Hodgkiss W, Song H, Kuperman W, Akal T, Ferla C and Jackson D 1999 A long range and variable phase conjugation experiment in shallow water *J. Acoust. Soc. Am.* **105** 1597–604
[36] Song H, Kuperman W, Hodgkiss W, Akal T and Ferla C 1999 Iterative time reversal in the ocean *J. Acoust. Soc. Am.* **105** 3176–84
[37] Draeger C and Fink M 1997 One-channel time reversal of elastic waves in a chaotic 2D-silicon cavity *Phys. Rev. Lett.* **79** 407–10
[38] Draeger C and Fink M 1999 One-channel time reversal in chaotic cavities: theoretical limits *J. Acoust. Soc. Am.* **105** 611–7
[39] Draeger C, Aime J-C and Fink M 1999 One-channel time reversal in chaotic cavities: experimental results *J. Acoust. Soc. Am.* **105** 618–25
[40] Dowling D 1992 Phase-conjugate array focusing in a moving medium *J. Acoust. Soc. Am.* **91** 3257–77
[41] Lund F and Rojas C 1989 Ultrasound as a probe of turbulence *Physica* D **37** 508–14
[42] Onsager L 1949 *Nuovo Cimento* **6** 249
[43] Roux P and Fink M 1995 Experimental evidence in acoustics of the violation of time reversal invariance induced by vorticity *Europhys. Lett.* **32** 25–9
[44] Roux P, de Rosny J, Tanter M and Fink M 1997 The Aharonov–Bohm effect revisited by an acoustic time reversal mirror *Phys. Rev. Lett.* **79** 3170–3
[45] Aharonov Y and Bohm D 1959 *Phys. Rev. Lett.* **115** 485–91
[46] Berry M V, Chambers R G, Large M D, Upstill C and Walmsley J C 1980 *Eur. J. Phys.* **1** 154–62
[47] Olariu S and Iovitzu Popescu I 1985 *Rev. Mod. Phys.* **57** 367–86
[48] Umeki M and Lund F 1996 Private communication
[49] Prada C, Wu F and Fink M 1991 The iterative time reversal mirror: a solution to self focusing in pulse-echo mode *J. Acoust. Soc. Am.* **90** 1119–29
[50] Prada C, Thomas J L and Fink M 1995 The iterative time reversal process: analysis of the convergence *J. Acoust. Soc. Am.* **97** 62–71
[51] Prada C and Fink M 1994 Eigenmodes of the time reversal operator: a solution to selective focusing in multiple target media *Wave Motion* **20** 151–63
[52] Thomas J L, Roux P and Fink M 1994 Inverse scattering analysis with an acoustic time reversal mirror *Phys. Rev. Lett.* **72** 637–40
[53] Prada C, Manneville S, Spoliansly D and Fink M 1996 Decomposition fo the time reversal operator: detection

and focusing on two scatterers *J. Acoust. Soc. Am.* **99** 2067–6
[54] Prada C and Fink M 1998 Separation of interfering acoustic scattered signals using the invariants of the time reversal operator: application to Lamb waves characterization *J. Acoust. Soc. Am.* **104** 801–7
[55] Mordant N, Prada C and Fink M 1999 Highly resolved detection and selective focusing in a waveguide using the DORT method *J. Acoust. Soc. Am.* **105** 2634–42
[56] White D N, Clark J M, Chesebrough J N, White M N and Campbell J K 1968 Effect of skull in degrading the display of echoencephalographic B and C scans *J. Acoust. Soc. Am.* **44** 1339–45
[57] Halliwell M and Mountford R A 1973 Physical sources of registration errors in pulse-echo ultrasonic systems I. Velocity and attenuation *Med. Biol. Eng.* **11** 27–32
[58] Mountford R A and Halliwell M 1973 Physical sources of registration errors in pulse-echo ultrasonic systems II. Beam deformation, deviation and divergence *Med. Biol. Eng.* **11** 33–8
[59] Phillips D J, Smith S W, von Ramm O T and Thurstone F L 1975 Sampled aperture techniques applied to B-mode echoencephalography *Acoust. Holography* **6** 103–20
[60] O'Donnell M and Flax S W 1988 Phase aberration measurements in medical ultrasound: human studies *Ultrason. Imag.* **10** 1–11
[61] Hirama M, Ikeda O and Sato T 1982 Adaptive ultrasonic array imaging system through an inhomogeneous layer *J. Acoust. Soc. Am.* **71** 100–9
[62] Hirama M and Sato T 1984 Imaging through an inhomogeneous layer by least-mean-square error fitting *J. Acoust. Soc. Am.* **75** 1142–7
[63] Flax S W and O'Donnell M 1988 Phase aberration correction using signals from point reflectors and diffuse scatters: basic principles *IEEE Trans. Ultrason. Ferroelec. Freq. Contr.* **35** 758–67
[64] O'Donnell M and Flax S W 1988 Phase aberration correction using signals from point reflectors and diffuse scatters: basic principles *IEEE Trans. Ultrason. Ferroelec. Freq. Contr.* **35** 768–74
[65] Trahey G E and Smith S W 1988 Properties of acoustical speckle in the presence of phase aberration I. First order statistics *Ultrason. Imag.* **10** 12–28
[66] Nock L, Trahey G E and Smith S W 1989 Phase aberration correction in medical ultrasound using speckle brightness as a quality factor *J. Acoust. Soc. Am.* **85** 1819–33
[67] Mallart R and Fink M 1991 The van Cittert–Zernike theorem in pulse echo measurements *J. Acoust. Soc. Am.* **90** 2718–27
[68] Mallart R and Fink M 1994 Adaptive focusing in scattering media through sound-speed inhomogeneities: the van Cittert–Zernike approach and focusing criterion *J. Acoust. Soc. Am.* **96** 3721–32
[69] Zhu Q, Steinberg B D and Arenson R 1993 Wavefront amplitude distortion and image side-lobe levels I. Theory and computer simulations *IEEE Trans. Ultrason. Ferroelec. Freq. Contr.* **40** 747–53
[70] Zhu Q, Steinberg B D and Arenson R 1993 Wavefront amplitude distortion and image side-lobe levels II. *in vivo* experiments *IEEE Trans. Ultrason. Ferroelec. Freq. Contr.* **40** 754–62
[71] Liu D-L and Waag R C 1994 Time-shift compensation of ultrasonic pulse focus degradation using least-mean-square error estimates of arrival time *J. Acoust. Soc. Am.* **95** 542–55
[72] Hinkelman L M, Liu D-L, Metlay L A and Waag R C 1994 Measurements of ultrasonic pulse arrival time and energy level variation produced by propagation through abdominal wall *J. Acoust. Soc. Am.* **95** 530–41
[73] Dorme C and Fink M 1995 Focusing in transmit–receive mode through inhomogeneous media: the time reversal matched filter approach *J. Acoust. Soc. Am.* **98** 1155–62
[74] Ikeda O 1989 An image reconstruction algorithm using phase conjugation for diffraction-limited imaging in an inhomogeneous medium *J. Acoust. Soc. Am.* **85** 1602–6
[75] Fink M and Dorme C 1996 Steering and focusing through inhomogeneous media with matched filter *IEEE Trans. Ultrason. Ferroelec. Freq. Contr.* **43** 167–75
[76] Ebbini E, Wang H, O'Donnell M and Cain C 1991 Acoustic feedback for hyperthermia phased-array applicators: aberration correction, motion compensation and multiple focusing in the presence of tissue inhomogeneities *Proc. IEEE Ultrason. Symp.* pp 1343–6
[77] Thomas J-L, Wu F and Fink M 1996 Time reversal focusing applied to lithotripsy *Ultrason. Imag.* **18** 106–21
[78] Thomas J-L and Fink M 1996 Ultrasonic beam focusing through tissue inhomogeneities with a time reversal mirror: application to transskull therapy *IEEE Trans. Ultrason. Ferroelec. Freq. Contr.* **43** 1122–9
[79] Tanter M, Thomas J-L and Fink M 1998 Focusing and steering through absorbing and aberrating layers: application to ultrasonic propagation through the skull *J. Acoust. Soc. Am.* **103** 2403–10
[80] Sun J and Hynynen K 1999 The potential of transskull ultrasound therapy and surgery using the maximum available skull surface area *J. Acoust. Soc. Am.* **105** 2519–27
[81] Kinsler L E, Frey A R, Coppens A B and Sanders J V 1982 *Fundamentals of Acoustics* (New York: Wiley)
[82] Liu D-L and Waag R C 1994 Correction of ultrasonic wavefront distortion using backpropagation and a reference waveform method for time-shift compensation *J. Acoust. Soc. Am.* **96** 649–60

[83] Beardsley B, Peterson M and Achenbach J D *J. Nondestructive Evaluation* **14** 169
[84] Chackroun N, Fink M and Wu F 1995 Time reversal processing in nondestructive testing *IEEE Trans. Ultrason. Ferroelec. Freq. Contr.* **42** 1087–98
[85] Miette V, Sandrin L, Wu F and Fink M 1996 Optimization of time reversal processing in titanium inspections *Proc. IEEE Ultrason. Symp. (San Antonio, USA)*